



Single-cell dissection of the genotype–immunophenotype relationship in glioblastoma

Nishant Soni,^{1,†} Kavita Rawat,^{2,†} Zhihong Chen,^{2,3} Angela DiMauro,² Bruno Giotti,¹
Dolores Hambardzumyan^{2,4} and Alexander M. Tsankov^{1,3,4}

[†]These authors contributed equally to this work.

Glioblastoma is the most aggressive and lethal adult brain tumour. The cellular heterogeneity within the tumour microenvironment plays a crucial role in the complexity of treatment and poor survival. Glioblastoma is typically classified into three molecular subtypes (classical, mesenchymal and proneural) associated with *EGFR*, *NF1* and *PDGFRA* genetic drivers, respectively. Yet, the role of these driver mutations in the glioblastoma tumour microenvironment is not fully understood. Here, we used single-cell RNA sequencing of genetically engineered mouse glioblastoma models incorporating human-relevant *EGFRvIII*, *PDGFB* and *NF1* driver mutations to characterize the genotype–immunophenotype relationship of the three glioblastoma subtypes systematically. Murine genetic glioblastoma models at the single-cell level effectively mimic the inter- and intra-tumour heterogeneity found in human counterparts.

Our analysis revealed that *PDGFB*-driven tumours were more proliferative and enriched for *Wnt* signalling interactions, whereas *EGFRvIII*-driven tumours showed an elevated interferon signalling response. Moreover, *Nf1*-silenced tumours displayed higher myeloid abundance, myeloid immunosuppressive interactions involving *Spp1*, regulatory T-cell infiltration and expression of immune checkpoint molecule *Ctla4*.

Overall, we established a human–mouse analytical platform for genotype-aware target discovery and validation, which offers promising new avenues for more effective, personalized treatments in glioblastoma.

- 1 Department of Genetics and Genomic Sciences, Icahn School of Medicine at Mount Sinai, New York, NY 10029, USA
- 2 Department of Oncological Sciences, The Tisch Cancer Institute, Icahn School of Medicine at Mount Sinai, New York, NY 10029, USA
- 3 Lipschultz Precision Immunology Institute, Icahn School of Medicine at Mount Sinai, New York, NY 10029, USA
- 4 Tisch Cancer Institute, Icahn School of Medicine at Mount Sinai, New York, NY 10029, USA

Correspondence to: Dolores Hambardzumyan
Icahn School of Medicine at Mount Sinai, Department of Oncological Sciences and Neurosurgery
1425 Madison Avenue, New York, NY 10029, USA
E-mail: dolores.hambardzumyan@mssm.edu

Correspondence may also be addressed to: Alexander M. Tsankov
Icahn School of Medicine at Mount Sinai, Department of Genetics and Genomic Sciences
New York, NY 10029, USA
E-mail: alexander.tsankov@mssm.edu

Keywords: single-cell genomics; glioblastoma; genetically engineered mouse models; tumour heterogeneity; myeloid cell diversity

Received October 31, 2024. Revised March 18, 2025. Accepted March 23, 2025. Advance access publication April 11, 2025

© The Author(s) 2025. Published by Oxford University Press on behalf of the Guarantors of Brain. All rights reserved. For commercial re-use, please contact reprints@oup.com for reprints and translation rights for reprints. All other permissions can be obtained through our RightsLink service via the Permissions link on the article page on our site—for further information please contact journals.permissions@oup.com.

Introduction

Glioblastoma (GBM), the most aggressive primary tumour in adults, exhibits pronounced inter- and intra-tumoural heterogeneity. Despite an aggressive multimodal standard of care for GBM, consisting of surgery, radiation therapy and temozolomide, the median survival of GBM patients remains low, at 13–24 months,¹ and the 5-year relative survival rate is only 6.8%.² Emerging immunotherapies, including immune checkpoint (IC) blockade and novel chimeric antigen receptor (CAR) T-cell therapies, although highly effective in other cancers, failed to provide a durable patient response in GBM clinical trials, except for rare cases of recurrent GBM.^{3–6} This is attributable, in part, to the highly immunosuppressive tumour microenvironment (TME), dominated by myeloid cells, consisting of neutrophils, monocytes, monocyte-derived macrophages (MDMs) and brain-resident microglia (MG) that in total make up ~30%–40% of GBM tumour mass.⁷ Recent evidence suggests that a high degree of inter- and intra-tumoural heterogeneity within the neoplastic compartment is associated with similar heterogeneity in the TME.⁸ Hence, a better understanding of the TME is urgently needed to elucidate the mechanisms driving increased heterogeneity and immunosuppression and to identify more effective therapeutic pathways in GBM.

To characterize the neoplastic inter-tumour heterogeneity of GBM, The Cancer Genome Atlas (TCGA) initiative provided robust gene expression-based identification of three GBM subtypes: proneural (PN), mesenchymal (MES) and classical (CL).^{9–12} These subtypes are not mutually exclusive and are determined by the dominant transcriptional patterns (determined by the abundance of cells with certain signatures) at the time and place of tumour resection. In fact, multiple subtypes can co-exist within a single tumour, whose relative proportion can evolve over time or in response to therapy.^{13,14} We demonstrated that although not mutually exclusive, aberrations in gene expression of epidermal growth factor receptor (EGFR), neurofibromin 1 (NF1) and platelet-derived growth factor receptor alpha (PDGFRA) were predominantly associated with the CL, MES and PN subtypes, respectively.^{15,16} This knowledge allowed us to generate human GBM-specific driver mutations using the RCAS/tv-a (Replication-Competent Avian Sarcoma-Leukosis virus/tumor virus receptor-A) gene transfer system to create immunocompetent genetically engineered mouse models (GEMMs) of murine GBM (mGBM) that share the same cell of origin. Although we and others have shown that these GEMMs closely mimic myeloid cell composition and bulk expression profiles observed in human GBM (hGBM) subtypes,^{16–19} it is equally important to identify species-specific differences in TME heterogeneity and at cellular resolution. Hence, we reasoned that single-cell characterization of mGBM models and comparison to hGBM would highlight the cross-species similarities/differences and enable investigators to identify and validate the most relevant human target candidates.

High-throughput, single-cell RNA sequencing (scRNA-seq) has greatly advanced our understanding of tumour heterogeneity in GBM.^{13,20,21} Neftel et al.²⁰ used scRNA-seq to show that malignant cells in GBM can be grouped into four distinct cellular states: neural progenitor-like (NPC-like), oligodendrocyte-progenitor-like (OPC-like), astrocyte-like (AC-like) and mesenchymal-like (MES-like) states. Although each GBM sample contains cells in multiple states, the proportion of cells in each state varies between tumours and is correlated with genetic alterations in EGFR, CDK4 and PDGFRA, in addition to mutations in NF1.²⁰ To determine whether there is a causal link between the main genetic drivers of GBM and TME heterogeneity, we performed scRNA-seq, multicolour

flow cytometry and in-depth computational analysis on EGFRvIII-driven, NF1-silenced and PDGFB-driven GEMMs to dissect the effect of common GBM genetic drivers on the TME (Fig. 1A). Our analytical strategy identified distinct TME cell composition, ligand–receptor interactions and gene expression modules associated with different GBM genetic drivers, which we validated with immunohistochemistry (IHC) and multiplexed flow analysis. To assess the human relevance, we compared our findings with bulk RNA-seq data from human GBM tumours¹² with mutually exclusive EGFRvIII deletion ($n = 10$), NF1 loss-of-function mutation ($n = 13$) or PDGFRA amplification on chromosome 4 ($n = 15$). Our integrative approach allowed us to shed light on the genotype-specific TME crosstalk, to catalogue the cross-species similarities/differences in GBM subtype tumour heterogeneity and to build a comprehensive resource and preclinical platform for systematic identification and validation of murine- and human-relevant GBM therapeutic targets in the appropriate genetic context.

Materials and methods

Mice used for the study

Ntv-a; EGFRvIII^{fl-stop-fl}, *Pten*^{fl/fl} and *Ntv-a* mice of both sexes (equal distribution) in the age range of 6–12 weeks were used for experiments.^{16,19,22} All animals were housed in a climate-controlled (18°C–23°C and 40%–60% humidity), pathogen-free facility, with access to food and water *ad libitum*, under a 12 h–12 h light–dark cycle.

RCAS virus propagation to generate *de novo* GBM

DF-1 cells (ATCC, CRL-12203) were purchased and grown at 39 °C according to the supplier's instructions. Cells were transfected with RCAS-PDGFB-HA, RCAS-PDGFA-myc, RCAS-shRNA-p53-Rfp, RCAS-shRNA-Nf1 and RCAS-shRNA-Pten-Rfp using a Fugene 6 transfection kit (Roche, 11814443001) according to the manufacturer's instructions. DF-1 cells (4×10^4) in 1 µl of Dulbecco's modified Eagle's medium were delivered stereotactically with a Hamilton syringe equipped with a 30-gauge needle for tumour generation. To generate PDGFB-driven GBM, a cocktail of RCAS-PDGFB-HA and RCAS-shRNA-p53-Rfp was injected into the right frontal striatum at the following coordinates: anteroposterior –1.5 mm and right –0.5 mm from bregma; depth –1.5 mm from the dura surface. To generate NF1-silenced tumours, a mixture of RCAS-shRNA-Nf1, RCAS-PDGFA-myc, RCAS-shRNA-p53-Rfp and RCAS-shRNA-Pten-Rfp was used. The injection site was aimed at the subventricular zone at the following coordinates: anteroposterior –0.0 mm and right –0.5 mm from bregma; depth –1.5 mm from the dura surface. For generation of EGFRvIII tumours, a mixture of DF-1 cells (4×10^4) that were infected with RCAS-Cre, RCAS-shRNA-p53-Rfp and RCAS-TAZ was co-injected at a 1:1:1 ratio in a final volume of 1 µl of Dulbecco's modified Eagle's medium. The target coordinates were aiming at the subventricular zone, with the at the following coordinates: anteroposterior –0.0 mm and right –0.5 mm from bregma; depth –1.5 mm from the dural surface.¹⁶ Mice were continually monitored for signs of tumour burden and were sacrificed upon observation of end-point symptoms, including head tilt, lethargy, seizures and excessive weight loss.

Spectral flow cytometry

Tumours were dissected from the brain, minced into pieces <1 mm³ and digested with 0.5% collagenase D (Sigma, 11088858001) and DNase I (Roche, 11284932001). Single-cell suspensions were passed

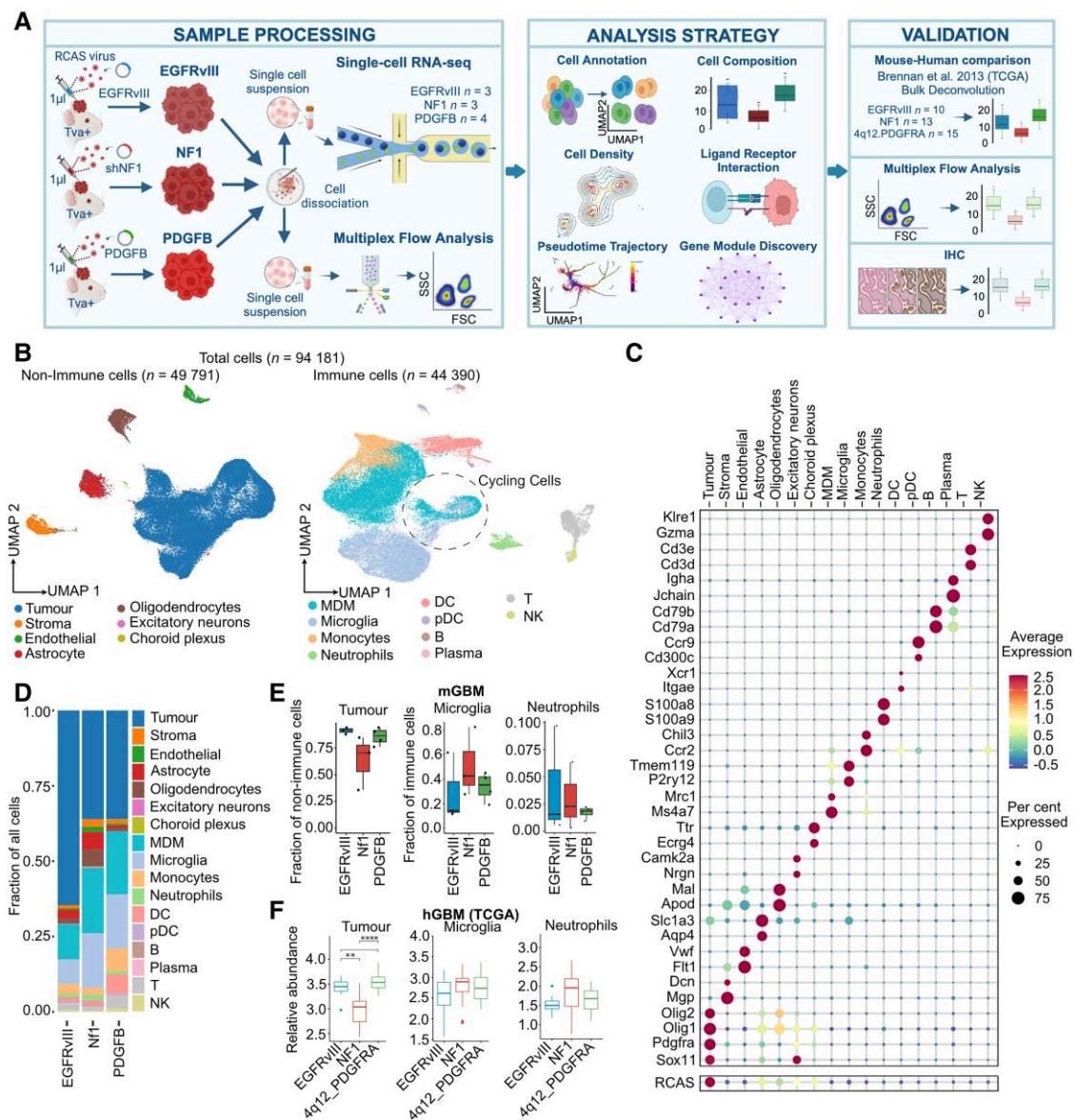


Figure 1 Single-cell RNA-sequencing catalogue of genetically engineered mouse models of glioblastoma with distinct genetic drivers. (A) Overview schematic of sample collection, tissue dissociation, cell sorting, sequencing, analysis workflow and validation cohorts. Created in BioRender. Tsankov, A. (2025) <https://BioRender.com/p31rjs0>. (B) Uniform manifold approximation and projection (UMAP) plot of all non-immune (left) and immune (right) cell single-cell RNA sequencing data in this study, coloured by cell-type annotations. (C) Dot plot showing expression levels and the percentage of cells expressing selected marker genes for each annotated cell type. (D) Stacked bar plots depicting proportion of annotated cells within each murine glioblastoma (mGBM) subtype. (E) Distribution of tumour cell abundance among non-immune cells, and distribution of microglia and neutrophil abundance among immune cells; t-test P-values were calculated. Blue = EGFRvIII, red = NF1 and green = PDGFB. Box plots display the median (central line) and interquartile range (box), with whiskers extending to the smallest and largest values within 1.5 times the interquartile range. Individual data points are shown as dots, providing a detailed view of the sample distribution. (F) Mean log₁₀ expression of tumour, microglia and neutrophil markers, split by genotype in human glioblastoma (hGBM) TCGA data, with Mann–Whitney–Wilcoxon test P-values calculated. Blue = EGFRvIII, red = NF1 and green = 4q12.PDGFB. Significance annotation: *P < 0.05, **P < 0.01, ***P < 0.001 and ****P < 0.0001. P-values > 0.05 are not shown. Box plots display the median (central line) and interquartile range (box), with whiskers extending to the smallest and largest values within 1.5 times the interquartile range. Points beyond this range are potential outliers and are shown as individual dots. DC = dendritic cells; FSC = forward scatter; IHC = immunohistochemistry; MDM = monocyte-derived macrophages; NK = natural killer cells; pDC = plasmacytoid DC; SSC = side scatter.

through 70 µm cell strainers, centrifuged, and resuspended in 30% Percoll (GE Healthcare, 17-0891-01) solution containing 10% fetal bovine serum (Hyclone SH30396.03). Cells were separated by centrifugation at 800g for 15 min at 4 °C. The supernatant was carefully removed to discard debris and myelin. The cells were then washed in cold phosphate buffered saline (PBS) and resuspended in red blood cell lysis buffer (BioLegend, 420301) for 1 min at 37 °C. Cells were then transferred to an Eppendorf tube and washed once with fluorescent

activated cell sorting (FACS) buffer [Dulbecco's PBS (DPBS) with 0.5% bovine serum albumin] and blocked with 100 µl of blocking solution [2% fetal bovine serum, 5% normal rat serum, 5% normal mouse serum, 5% normal rabbit serum, 10 µg/ml anti-FcR (BioLegend, 101319) and 0.2% NaN₃ in DPBS] on ice for 30 min. Cells were then stained with primary antibodies (Supplementary Table 1; 1:100 dilution) on ice for 30 min and washed with PBS. The cells were subsequently incubated in 100 µl of viability dye (Zombie UV, BioLegend, 1:800) at

room temperature for 20 min, washed, and fixed with fixation buffer (eBioscience, 00-5123-43, 00-5223-56) for 30 min at 4 °C. Cells stained for lymphoid markers were then permeabilized with a permeabilization buffer (eBioscience, 00-8333-56) before the intracellular markers were stained. All data were collected on a Cytek Aurora spectral flow cytometer, and data were analysed offline using FlowJo v.10 software (Tree Star Inc., RRID:SCR_008520).

Tissue processing and immunohistochemistry

To process mouse tumour tissues, animals were anaesthetized with ketamine and xylazine and perfused transcardially with ice-cold Ringer solution. Brains were removed and processed according to the different applications. For haematoxylin and eosin tumour validation and IHC staining, brains were fixed in 10% neutral buffered formalin for 72 h at room temperature, processed in a tissue processor (Leica, TP1050), embedded in paraffin, sectioned at 5 µm thickness with a microtome (Leica) and mounted on superfrost glass slides (ThermoFisher 3039-002). Slides were rehydrated with tap water and dipped in haematoxylin (ThermoFisher, 7231), bluing agent (ThermoFisher, 22-220-106) and eosin (ThermoFisher, M1098442500) for 1 min each, with thorough washes with tap water in between. Slides were dehydrated with series washes in ethanol and Neo-clear (ThermoFisher, M1098435000) before being mounted in Permount medium (ThermoFisher, SP15-100).

For validation of hypoxic regions, anti-GLUT-1 (1:400, Cell Signaling, 129395) and anti-HIF-1α (1:400, Cell Signaling, 480855) were used, whereas to validate macrophage and neutrophil infiltration in the pseudopalisading areas, anti-IBA-1 (1:500, Wako, 019-19741) and anti-ELANE (1:400, Abcam, ab68672) were used, respectively (Supplementary Table 1). To validate the proliferating cells in the different GBM subtypes, we used anti-phosphorylated Histone 3 (pHH3) (1:400, Millipore, 06-570). To validate ligand–receptor interactions, we performed IHC stainings with antibodies for WNT5A, LRP5, CD44 and SPP1. WNT5A and LRP5 IHC stainings were performed on the Discovery Ultra platform (Roche), whereas CD44, SPP1, ELANE, GLUT1, IBA1 and HIF-1α stainings were performed on the Leica Bond Rx platform (Leica). Appropriate primary and secondary antibodies (Supplementary Table 1) were purchased from Leica, BD, Cell signaling, Santa Cruz or Invitrogen.

Image analysis

Stained tissue sections were scanned at ×20 and converted to digital images using a Nanozoomer 2.0HT whole slide scanner (Hamamatsu Photonic K.K.) and observed offline with NDP view2 software (Hamamatsu). For each staining and sample, five representative images were acquired to represent the tumour area accurately. For WNT5A, LRP5, CD44 and SPP1, the percentage of positively stained tumour area was calculated using the threshold function in ImageJ Fiji79 software by recording the difference between positive staining intensity above background staining intensity. For phospho-histone 3, the number of positively stained nuclei per millimetre squared was quantified. All image analysis was performed using ImageJ Fiji. Statistical analysis and graphs were created using GraphPad Prism v.9.

Single-cell RNA sequencing and analysis

ScRNA-seq tissue dissociation, data processing and analysis were performed as described previously^{23,24} (see the Supplementary material, 'Methods' section). Briefly, GBM tumours were dissected from whole mouse brain, dissociated into single-cell suspensions, and single-cell sequenced using the Chromium platform (10X

Genomics).^{23,24} Raw FASTQ files were aligned to the mouse genome reference mm10, customized to include the Rfp and RCAS sequence, using Cell Ranger (v.5.0.0). Subsequent data processing and analysis were performed using the Seurat package (v.4.3.0),²⁵ and most figures were plotted using the R package ggplot2 (v.3.5.0). We used Seurat's CellCycleScoring function to classify cells with S or G2/M phase scores > 0.10 as cycling and the rest as non-cycling. Neftel cell-state signatures were mapped to mouse orthologues, scored using Seurat's AddModuleScore function and presented as a 2D scatter plot, as previously described by Neftel et al.²⁰

To identify differentially expressed genes across mGBM samples, we used the R package muscat (v.1.12.1),²⁶ which implements the DESeq2 method. To identify co-expressed network gene modules, we used the R package high-dimensional weighted gene co-expression network analysis (hdWGCNA)²⁷ (v.1.72). To uncover significantly enriched pathways within the gene modules and differential genes, we performed a pathway enrichment analysis using the R package clusterProfiler (v.4.6.2).²⁸ Density plots were generated using the LSD R package.²⁹ We inferred ligand–receptor interactions using CellPhoneDB (v.2.1.7; database v.4.0.0).³⁰

All RNA velocity analyses were performed using the scVelo package (v.0.3.2, Python 3.9.13) with default parameter settings. RNA velocity is a statistical inference of cell-state transitions and does not have the ability to trace lineages or predict causal relationships between cell populations.

Human, bulk RNA-sequencing data procurement and analysis

We retrieved bulk RNA-seq and somatic mutation data for TCGA glioblastoma from cBioPortal³¹ using the cgdsr package in R. From this study, we separated GBM samples into PN, CL and MES GBM subtypes as done previously.¹² Next, we selected CL samples with EGFRvIII mutation (*n* = 10), MES samples with NF1 mutation (*n* = 13) and PN samples with 4q12_PDGFRα amplification (*n* = 15), for which we included only samples with mutually exclusive mutations (i.e. no co-mutations). For deconvolution analysis, signature scores were calculated for each gene set by computing the mean log₁₀ expression of all genes, allowing us to evaluate the activity of scRNA-seq programmes and relative abundance of cell types in the TCGA bulk RNA-seq data.

Quantification and statistical analyses

All statistical analyses are described in the figure legends. The P-values were typically calculated using Student's t-test (Gaussian-distributed data) and the Mann–Whitney–Wilcoxon test (non-Gaussian-distributed data). For quantifying differential enrichment of ligand–receptor interactions between two groups, we calculated P-values using Fisher's exact test.

Results

ScRNA-seq catalogue of murine GBM with distinct genetic drivers

To dissect the relationship between different GBM genetic drivers and the TME, we used the RCAS/tv-a gene transfer system to create immunocompetent GEMMs of GBM originating from Nestin⁺ cells.^{15,16} To model PN and CL mGBM, we overexpressed human PDGFB construct and induced tumour cell-specific expression of EGFRvIII, respectively, and to model MES hGBM, we silenced endogenous Nf1^{23,24} (hereafter referred to as EGFRvIII, PDGFB and Nf1

mGBM, respectively). We performed high-throughput scRNA-seq on mGBM tumours isolated from murine brains (three or four biological replicates for each GEMM), resulting in a total of 94 181 cells after removal of doublets and low-quality cells (see the 'Materials and methods' section; Fig. 1B, Supplementary Fig. 1A and Supplementary Table 2). Next, we performed unsupervised clustering and systematically annotated cell clusters based on the consistent expression of known cell-type markers (Fig. 1C). As expected, tumour cells were marked by high expression of the RCAS gene (Fig. 1C, bottom). Subsequently, we identified more fine-grained cell subsets by repeated clustering and annotation within each cellular compartment (Supplementary Fig. 1B).

Examining the cellular composition of different GEMMs showed remarkable TME heterogeneity associated with different genetic drivers (Fig. 1D and Supplementary Fig. 1C). Specifically, we observed higher fractions of tumour cells in *EGFRvIII* and *PDGFB* mGBM than in *Nf1* mGBM (Fig. 1E), which was corroborated by bulk deconvolution analysis of human GBM tumours with similar genetic make-up (Fig. 1F). In contrast, *Nf1/NF1*-deactivated tumours had higher abundance of MG and neutrophils in both mGBM and hGBM (Fig. 1E and F). Hence, scRNA-seq results of our GEMMs demonstrate a close resemblance to both the inter-tumour and intra-tumoural heterogeneity observed in hGBM, thus giving us confidence to dive deeper into the cellular phenotypes that differ between GBM genetic drivers, starting with neoplastic cells.

Increased proliferation and WNT signalling in *PDGFB*-driven GBM

When examining the 43 675 tumour cells in our scRNA-seq data, we observed distinct patterns of cancer-intrinsic heterogeneity between GEMMs of GBM (Fig. 2A and Supplementary Fig. 2A). Most prominently, we observed a significant enrichment of proliferating/cycling cells in *EGFRvIII* and *PDGFB* mGBM versus *Nf1* mGBM (Fig. 2B), where tumour cells were classified as cycling if they exhibited high scores for either S or G2/M phase marker signatures (Fig. 2A and 'Materials and methods' section). The cell cycle proliferation trends between different GBM genetic drivers were also similar in our human GBM bulk RNA-seq validation cohort (Fig. 2C). To substantiate our observations further, we conducted immunostaining of mouse tumour samples with the proliferation marker phosphorylated histone H3 (PHH3), which labelled cells in the M-phase of the cell cycle and revealed markedly increased cell cycle activity in *PDGFB* mGBM samples (Fig. 2D and Supplementary Fig. 2B).

To delve deeper into the potential mechanisms driving higher cell cycle activity in *PDGFB* mGBM, we inferred ligand–receptor interactions³² occurring between tumour cells and other cell types across different genotypes (Supplementary Fig. 2C). Our analysis revealed consistent enrichment of interactions involving *Wnt5a* and its corresponding receptors, including *Ror1*, *Ror2*, *Ptprk*, *Frzb*, *Epha7*, members of the *Frizzled* (*Fzd4*, *Fzd6*, *Fzd7* and *Fzd8*) and *LDLR* (*Lrp5* and *Lrp6*) gene families, exclusively in *PDGFB* mGBM (Fig. 2E and Supplementary Fig. 2C). Earlier experiments in glioma cell lines demonstrated a coupling between WNT signalling and cell proliferation,³³ suggesting that increased *Wnt5a* interactions in *PDGFB* mGBM contribute to a more proliferative phenotype. To investigate whether the increased Wnt signalling interactions were attributable to higher expression of the relevant ligands or receptors, we performed differential expression analysis²⁶ for Wnt pathway genes across all annotated cell types (Supplementary Fig. 3A). Our analysis revealed that *Wnt5a* was highly upregulated in *PDGFB* mGBM malignant cells along with *Wnt7b* (Fig. 2F), which

probably contributes to the increased Wnt interactions in *PDGFB* mGBM (Fig. 2E). This finding was corroborated by hGBM RNA-seq data, where we observed elevated expression levels of *WNT5A* and *WNT7B* in *PDGFRA*-amplified tumours (Fig. 2G). We note that several receptors were differentially expressed in *PDGFB* mGBM tumour cells, including *Ror2*, *Fzd3*, *Fzd4* and *Fzd8* (Supplementary Fig. 3A and B), but these trends were not conserved in our hGBM validation cohort (Supplementary Fig. 3C). To validate our findings experimentally, we performed IHC on five independent tumours per genotype using antibodies for *WNT5A* and *LRP5* (Fig. 2H and I and Supplementary Fig. 4A). Our analysis revealed a significantly higher percentage of tumour area with positive staining for both *WNT5A* and *LRP5* in *PDGFB* mGBM relative to other mGBM subtypes, confirming our results from the scRNA-seq data at the protein level. In sum, we observed and experimentally validated increased WNT signalling expression and tumour cell proliferation in *PDGFB* mGBM, suggesting future studies to explore the direct link between Wnt signalling and cell proliferation *in vivo*.

Cancer-intrinsic heterogeneity associated with different genetic alterations

To investigate the intratumoural heterogeneity of neoplastic cells, we scored our scRNA-seq data for the four GBM cellular state signatures defined by Neftel et al.²⁰ Our analysis demonstrated that the four hGBM cellular states are also expressed in our murine models in a genotype-specific manner (Fig. 2J and Supplementary Fig. 4B). Namely, a higher prevalence of MES/AC-like cells was found in *Nf1* mGBM, whereas NPC/OC-like cells were more abundant in *PDGFB* mGBM; finally, *EGFRvIII* mGBM fell in between those two trends (Fig. 2K). These results were highly concordant with our hGBM validation cohort (Fig. 2L) and findings from prior studies.^{15,16,20} Hence, we provide direct evidence that driver mutations contribute to defining the abundance of various neoplastic cellular states in GBM.

To discover *de novo* malignant cell programmes in mGBM, we conducted hdWGCNA²⁷ and identified 14 mGBM-specific programmes (Supplementary Table 3). Among these, three malignant cell programmes showed enrichments for different genotypes that were consistent with our hGBM validation cohort (Supplementary Fig. 4D and E). Specifically, *Nf1* mGBM tumours showed elevated expression in tumour necrosis factor alpha (TNF α) signalling, *EGFRvIII* mGBM exhibited higher expression of interferon alpha/gamma signalling, and *PDGFB* mGBM displayed increased expression in G2/M-phase cell cycle programme in mGBM and hGBM (Supplementary Fig. 4D and E). As additional validation, the corresponding Hallmark TNF α , Interferon (both type I and type II) signalling and G2/M-phase checkpoint cancer programmes demonstrated consistent expression patterns across mGBM models as the mGBM-specific programmes (Supplementary Fig. 4F). Taken together, our GEMMs demonstrate genotype-specific enrichments for malignant cell states and cancer-intrinsic expression programmes, including cell proliferation, TNF α and interferon signalling, which is highly concordant with those observed in hGBM.

Tumour genotype dictates myeloid cell composition and chemokine expression profiles

Myeloid cells are the most abundant non-neoplastic cell class in the GBM TME and play a major role in tumourigenesis and immunosuppression, limiting the efficacy of various treatment regimens, including immunotherapies.^{34–36} Despite their crucial role in GBM, the dynamics of myeloid cells during disease progression and

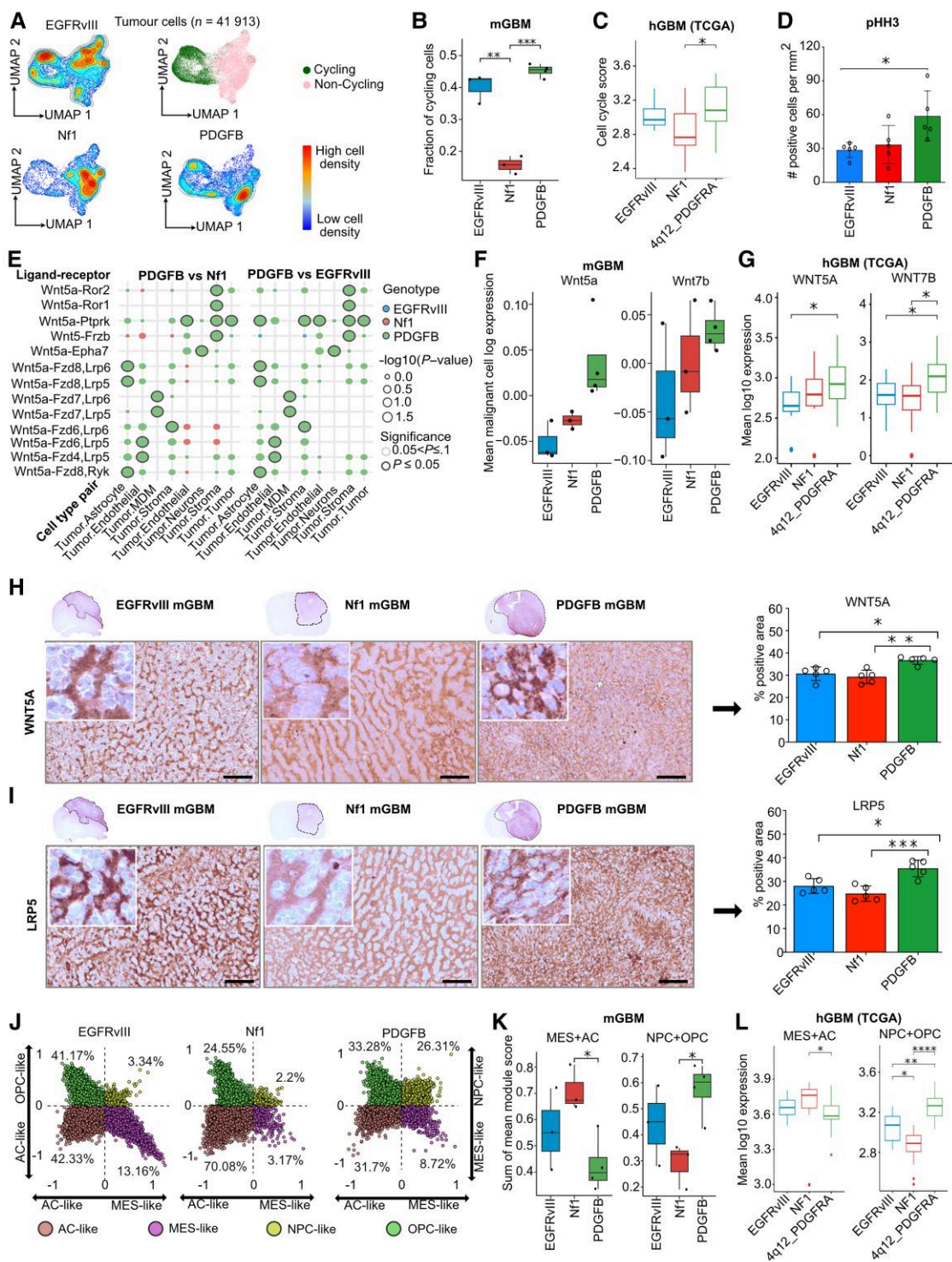


Figure 2 Distinct cancer-intrinsic expression programmes and signalling pathways are associated with different genetic drivers of murine glioblastoma. (A) Uniform manifold approximation and projection (UMAP) plots of all tumour cells coloured by cell cycle status (top right) or by cell density (others) for the three genetically engineered mouse models (GEMMs), where red indicates high cell density and blue indicates low density. (B) Distribution of fraction of cycling tumour cells across replicates for each GEMM; t-test P-values were calculated. Blue = EGFRvIII, red = NF1 and green = PDGFB. Box plots display the median (central line) and interquartile range (box), with whiskers extending to the smallest and largest values within 1.5 times the interquartile range. Individual data points are shown as dots, providing a detailed view of the sample distribution. (C) Mean log₁₀ expression of cycling marker genes, split by genotype in human glioblastoma (hGBM) TCGA data, with Mann-Whitney-Wilcoxon test P-values calculated. Blue = EGFRvIII, red = NF1 and green = 4q12_PDGFB. Significance annotation: *P < 0.05, **P < 0.01, ***P < 0.001 and ****P < 0.0001. P-values > 0.05 are not shown. Box plots display the median (central line) and interquartile range (box), with whiskers extending to the smallest and largest values within 1.5 times the interquartile range. Points beyond this range are potential outliers and are shown as individual dots. (D) Immunohistochemistry (IHC) analysis of murine glioblastoma (mGBM) tumours stained with the proliferation marker phosphorylated histone H3 (pHH3), split by GEMM subtype, with t-test P-values calculated. Blue = EGFRvIII, red = NF1 and green = PDGFB. (E) Dot plot of differential ligand-receptor

(Continued)

dependence on genetic drivers remain poorly understood.^{24,37} To explore the different populations of myeloid cells in GBM, we performed fine-grained cell annotation based on the expression of canonical markers and detected MG (*P2ry12* and *Tmem119*), MDMs (*Ms4a7* and *Mrc1*), monocytes (*Ccr2* and *Chil3*), neutrophils (*S100a9* and *S100a8*), dendritic cells (DCs; *Itgae* and *Xcr1*), plasmacytoid DCs (pDCs; *Cd300c* and *Klk1*) and a population of proliferating MG/MDM expressing *Mki67* (Figs 1C and 3A and Supplementary Fig. 5A). Relative to all myeloid cells, we observed a higher abundance of MDMs, MG and neutrophils in *Nf1* mGBM, whereas DCs and monocytes were increased in PDGFB mGBM (Fig. 3B and Supplementary Fig. 5B). Given that these findings were based on limited sample size (three or four replicates) of our scRNA-seq data, we conducted multicolour flow cytometry analysis on a larger mGBM cohort (19 tumours; 7 *EGFRvIII*, 5 *Nf1* and 7 PDGFB mGBM), which largely validated our initial observations (Fig. 3C).

To gain a better understanding of the mechanisms driving genotype-dependent differential myeloid recruitment, we compared the chemokine expression profiles of mGBM tumour subtypes. Chemokines play a crucial role in myeloid cell recruitment and activation within the GBM TME, which significantly impacts tumour progression and immune responses.³⁸ Our scRNA-seq data showed genotype-specific chemokine expression profiles (Supplementary Fig. 5C). Specifically, *Nf1* mGBM and, to a lesser degree, PDGFB mGBM were characterized by higher expression of monocyte chemoattractant family (MCP) ligands *Ccl2/3/4/5/7/8/12* in MG and when aggregated across all myeloid cells (Fig. 3D and Supplementary Fig. 5D, top), implicating these chemokines in enhanced monocyte/MDM recruitment in these tumours in comparison to *EGFRvIII* mGBM (Fig. 3C). Moreover, the hGBM validation cohort showed highly similar trends in MCP family expression and monocyte/MDM abundance across these three genotypes (Fig. 3E and F and Supplementary Fig. 5D, bottom). Overall, these findings demonstrate the genotype-dependent chemokine landscapes in GBM subtypes, which contribute to the unique myeloid cell recruitment, composition and expression programmes.

Microglia diversity, phenotypes and cell-state transitions in mGBM

Microglia are unique myeloid cells of the CNS that originate exclusively from erythro-myeloid progenitor cells in the yolk sac during

embryogenesis³⁹ and display a long life span (15 months on average) and low rates of self-renewal.^{40–43} Recent advances in single-cell technologies, such as cytometry by time-of-flight and scRNA-seq, have unveiled the complex heterogeneity of human and murine microglia in health and disease.^{44,45} To investigate the diversity of microglia in mGBM subtypes, we categorized 14 214 MG cells into five populations expressing established markers: proliferating (*Top2a* and *Mki67*), disease-associated (*Gpnmb* and *Spp1*), homeostatic (*P2ry12* and *Tmem119*), interferon-responsive (*Ifit1* and *Ifit2*) and pro-inflammatory MG (*Il1a* and *Il1b*; Fig. 3G and H). Relative to all MG, proliferating MG were more abundant in *EGFRvIII* mGBM, whereas homeostatic MG were elevated in *Nf1* mGBM (Fig. 3I and Supplementary Fig. 6A). Moreover, disease-associated MG showed relatively higher levels in PDGFB mGBM and *EGFRvIII* mGBM, and pro-inflammatory MG were enriched in both *Nf1* and PDGFB mGBM (Fig. 3I). As a complementary analysis, we identified *de novo* 13 co-expressed gene modules in MG using hdWGCNA (Supplementary Table 4). We found four MG programmes (proliferation, hypoxia, interferon and TNF α signaling) that were expressed specifically in the annotated MG subpopulations and showed highly similar mGBM subtype enrichments (Supplementary Fig. 6B–D). Interestingly, the hypoxia programme was predominantly expressed in disease-associated MG. We found that hypoxic areas in tumours attract and retain tumour-associated macrophages and cytotoxic T lymphocytes. In these hypoxic niches, immune cells undergo a reprogramming process that leads to an immunosuppressive state.⁴⁶ Because we have observed an increased presence of hypoxia-related gene signatures in disease-associated MG, it is likely that these MG reside in hypoxic niches of glioblastoma. To investigate the potential dynamics in MG state transitions, we inferred cell trajectories using RNA velocity.⁴⁷ The inferred vector fields suggest that homeostatic and disease-associated microglia converge towards a pro-inflammatory phenotype (Fig. 3J). Overall, we characterized the MG cell-state diversity and dynamics in mGBM and found genotype-associated MG subpopulations and expression programmes.

Immunosuppressive MDM modules, cell interactions linked to *Nf1* mGBM

Monocytes from blood circulation are recruited to the tumour site, where they differentiate into MDMs.^{7,48,49} These cells play a crucial

Figure 2 Continued

interactions between tumour cells and other cell classes, where blue indicates enrichment in *EGFRvIII*, red indicates enrichment in *Nf1*, and green indicates enrichment in PDGFB tumour samples. No outline indicates a P -value > 0.1 , grey outline indicates $0.05 < P \leq 0.1$, and black outline indicates $P \leq 0.05$ as assessed by Fisher's exact test. (F) Average *Wnt5a* and *Wnt7b* gene log expression in tumour cells, split by mGBM genotype, with Mann–Whitney–Wilcoxon test P -values calculated. Blue = *EGFRvIII*, red = *Nf1* and green = PDGFB. Box plots display the median (central line) and interquartile range (box), with whiskers extending to the smallest and largest values within 1.5 times the interquartile range. Individual data points are shown as dots, providing a detailed view of the sample distribution. (G) Mean \log_{10} expression of *WNT5A* and *WNT7B* genes, split by genotype in hGBM TCGA data, with Mann–Whitney–Wilcoxon test P -values calculated. Blue = *EGFRvIII*, red = *NF1* and green = *4q12_PDGFRA*. Significance annotation: * $P < 0.05$, ** $P < 0.01$, *** $P < 0.001$ and **** $P < 0.0001$. P -values > 0.05 are not shown. Box plots display the median (central line) and interquartile range (box), with whiskers extending to the smallest and largest values within 1.5 times the interquartile range. Points beyond this range are potential outliers and are shown as individual dots. (H and I) Left: Representative images of immunohistochemical staining using antibodies for *WNT5A* (H) and *LRP5* (I) on *EGFRvIII*, *Nf1* and PDGFB mGBM tumour sections. Right: Bar graphs showing the percentage of tumour area with positive staining after quantification ($n = 5$ biological replicates), where one-way ANOVA with Tukey's post hoc test was used. * $P < 0.05$, ** $P < 0.02$ and *** $P < 0.001$. Scale bars: 100 μm . (J) 2D quadrant scatter plot representing the GBM cellular state defined by Neftel et al.²⁰ across tumour cells split by mGBM genotype, where orange colour indicates astrocyte (AC)-like, purple colour indicates mesenchymal (MES)-like, yellow indicates neural progenitor (NPC)-like and green indicates oligodendrocyte-progenitor (OPC)-like cells. (K) Sum of average MES- and AC-like scores (left) and sum of average NPC- and OPC-like scores (right) across samples split by mGBM genotype, with t-test P -values calculated. Blue = *EGFRvIII*, red = *Nf1* and green = PDGFB. Box plots display the median (central line) and interquartile range (box), with whiskers extending to the smallest and largest values within 1.5 times the interquartile range. Individual data points are shown as dots, providing a detailed view of the sample distribution. (L) Sum of average MES- and AC-like scores (mean \log_{10} expression; left) and NPC- and OPC-like scores (right) across samples split by hGBM genotype in TCGA data, with Mann–Whitney–Wilcoxon test P -values calculated. Blue = *EGFRvIII*, red = *NF1* and green = *4q12_PDGFRA*. Box plots display the median (central line) and interquartile range (box), with whiskers extending to the smallest and largest values within 1.5 times the interquartile range. Points beyond this range are potential outliers and are shown as individual dots.

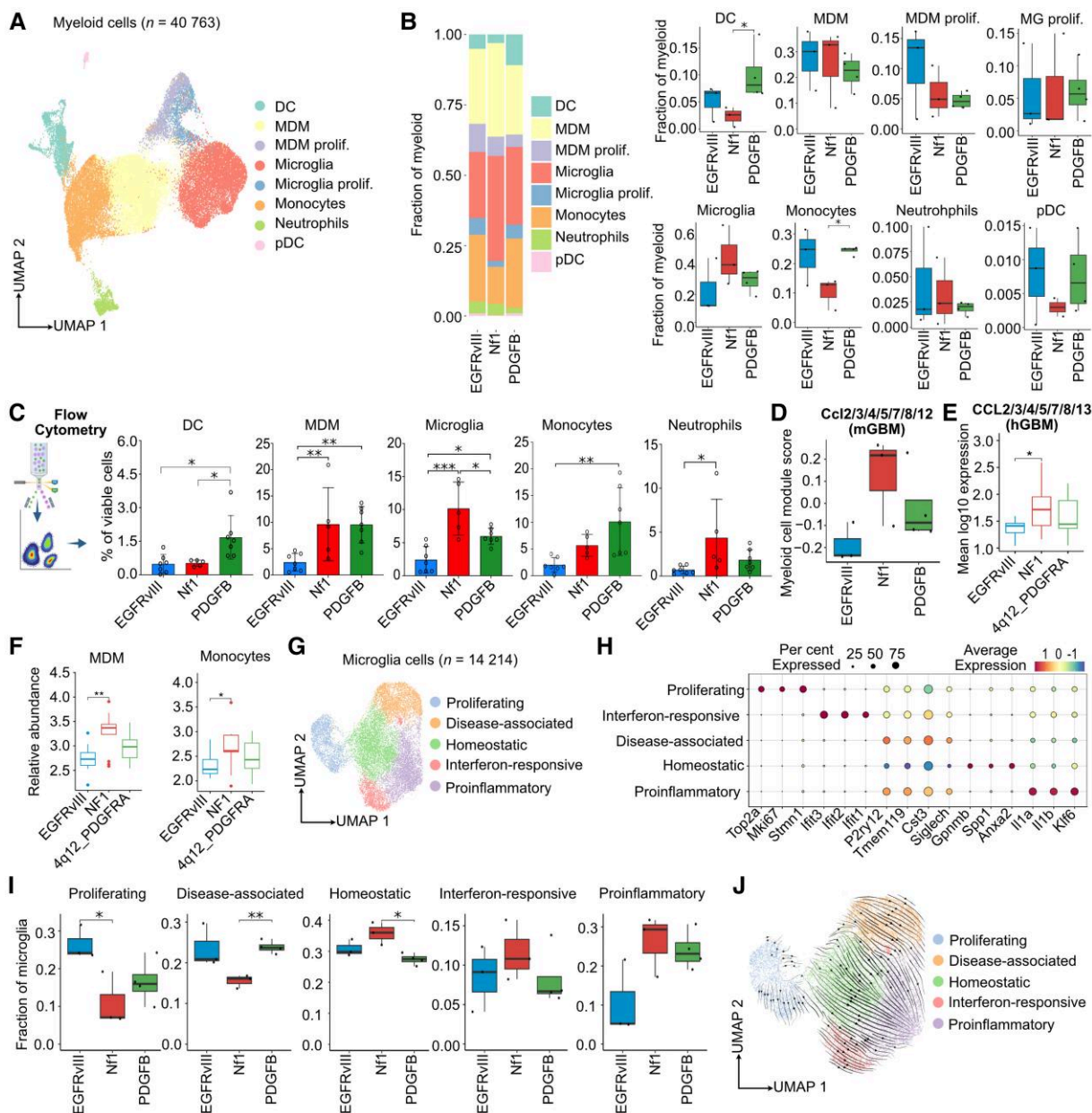


Figure 3 Genotype-dependent myeloid cell composition, microglia diversity and phenotypes. (A) Uniform manifold approximation and projection (UMAP) plot of all sequenced murine glioblastoma (mGBM) myeloid cells, coloured by annotated myeloid cell subset. (B) Stacked bar plots depicting the proportion of annotated myeloid cell subsets (left) and box plots showing the cell subset abundance distribution across samples within each mGBM genotype (right). The t-test P-values were calculated. Blue = EGFRvIII, red = NF1 and green = PDGFB. Box plots display the median (central line) and interquartile range (box), with whiskers extending to the smallest and largest values within 1.5 times the interquartile range. Individual data points are shown as dots, providing a detailed view of the sample distribution. (C) Flow cytometry analysis of mGBM samples myeloid cell distribution. The t-test P-values were calculated. Blue = EGFRvIII, red = NF1 and green = PDGFB. (D) Monocyte chemoattractant family ligands *Ccl2*, *Ccl3*, *Ccl4*, *Ccl5*, *Ccl7*, *Ccl8* and *Ccl12*, with average expression scores calculated across myeloid cells for each sample grouped by mGBM genotype. Mann-Whitney-Wilcoxon test P-values were calculated, with blue = EGFRvIII, red = NF1 and green = PDGFB. Box plots display the median (central line) and interquartile range (box), with whiskers extending to the smallest and largest values within 1.5 times the interquartile range. Individual data points are shown as dots, providing a detailed view of the sample distribution. (E) Monocyte chemoattractant family ligands *CCL2*, *CCL3*, *CCL4*, *CCL5*, *CCL7*, *CCL8* and *CCL13*, with mean log₁₀ expression calculated for each sample grouped by human glioblastoma (hGBM) genotype. Mann-Whitney-Wilcoxon test P-values were calculated, with EGFRvIII in blue, NF1 in red and 4q12_PDGFRA in green. Box plots display the median (central line) and interquartile range (box), with whiskers extending to the smallest and largest values within 1.5 times the interquartile range. Points beyond this range are potential outliers and are shown as individual dots. (F) Mean log₁₀ expression of monocyte-derived macrophage (MDM) and monocyte marker genes for samples, split by genotype in hGBM TCGA data, with Mann-Whitney-Wilcoxon test P-values calculated. Blue = EGFRvIII, red = NF1 and green = 4q12_PDGFRA. Significance annotation: *P < 0.05, **P < 0.01, ***P < 0.001 and ****P < 0.0001. P-values > 0.05 are not shown. Box plots display the median (central line) and interquartile range (box), with whiskers extending to the smallest and largest values within 1.5 times the interquartile range. Points beyond this range are potential outliers and are shown as individual dots. (G) UMAP plot of all mGBM microglia cells coloured by annotated microglia (MG) subsets. (H) Dot plot showing expression levels and the percentage of cells expressing selected marker genes for each annotated MG subset. (I) Distribution of microglia subset proportions, split by mGBM genotype. The t-test P-values were calculated, with blue = EGFRvIII, red = NF1 and green = PDGFB. Box plots display the median (central line) and interquartile range (box), with whiskers extending to the smallest and largest values within 1.5 times the interquartile range. Individual data points are shown as dots, providing a detailed view of the sample distribution. (J) UMAP plot of RNA velocity cell-state transition in MG cells, coloured by MG cell subsets. DC = dendritic cells; pDC = plasmacytoid DC.

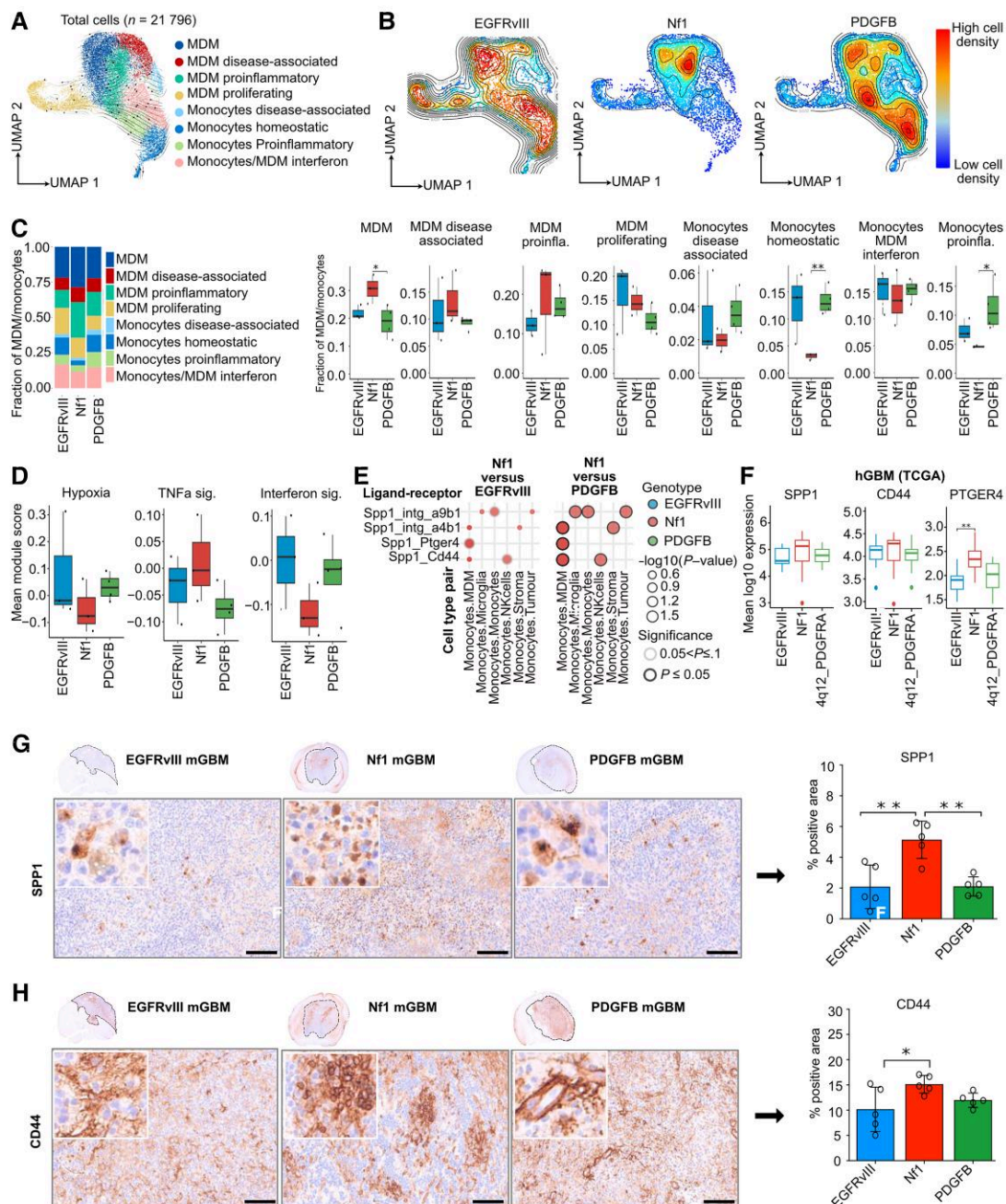


Figure 4 Characterization of monocyte and monocyte-derived macrophage heterogeneity across murine glioblastoma subtypes. (A) Uniform manifold approximation and projection (UMAP) plot of all sequenced murine glioblastoma (mGBM) monocytes and monocyte-derived macrophages (MDMs), coloured by subset annotations. (B) UMAP plot of MDMs/monocytes coloured by cell density for each GEMM, with red indicating high cell density and blue indicating low density. (C) Left: stacked bar plots depicting the proportion of MDMs/monocyte subsets for each mGBM subtype, coloured by cell type. Right: box plots showing the distribution of MDM/monocyte subset proportions split by mGBM genotype; t-test P-values were calculated, with EGFRvIII, red = Nf1 and green = PDGFB. Box plots display the median (central line) and interquartile range (box), with whiskers extending to the smallest and largest values within 1.5 times the interquartile range. Individual data points are shown as dots, providing a detailed view of the sample distribution. (D) Box plots showing the average scores for MDM/monocyte mGBM-specific programmes identified by high-dimensional weighted gene co-expression network analysis (hdWGCNA) in mGBM samples split by genotype. Mann-Whitney-Wilcoxon test P-values were calculated, with EGFRvIII in blue, Nf1 in red, and PDGFB in green. Box plots display the median (central line) and interquartile range (box), with whiskers extending to the smallest and largest values within 1.5 times the interquartile range. Individual data points are shown as dots, providing a detailed view of the sample distribution. (E) Dot plot of differential ligand-receptor interactions between MDMs/monocytes and other cell classes, where blue indicates enrichment in EGFRvIII, red indicates enrichment in Nf1, and green indicates enrichment in PDGFB tumour samples. No outline indicates a P-value > 0.1, grey outline indicates $0.05 < P \leq 0.1$, and black outline indicates $P \leq 0.05$ as assessed by Fisher's exact test. (F) Mean log₁₀ expression of SPP1, CD44 and PTGER4 genes, split by genotype in human GBM (hGBM) TCGA data, with Mann-Whitney-Wilcoxon test P-values calculated. Blue = EGFRvIII, red = Nf1 and green = 4q12_PDGFRA. Significance annotation: * $P < 0.05$, ** $P < 0.01$, *** $P < 0.001$ and **** $P < 0.0001$. P-values > 0.05 are not shown. Box plots display the median (central line) and interquartile range (box), with whiskers extending to the smallest and largest values within 1.5 times the interquartile range. Points beyond this range are potential outliers and are shown as individual dots. (G and H) Left: Representative images of immunohistochemical staining using antibodies for SPP1 (G) and CD44 (H) on EGFRvIII, Nf1 and PDGFB mGBM sections. Right: Bar graphs showing the percentage of tumour area with positive staining after quantification, where one-way ANOVA with Tukey's post hoc test was used; * $P < 0.05$ and ** $P < 0.02$. Scale bars: 100 μ m.

role in tumour progression by releasing various growth factors and cytokines that support tumour growth and suppress anti-tumour immune responses.^{7,50,51} To elucidate the diversity of monocytes and MDMs in our scRNA-seq data, we performed unsupervised clustering and identified eight cell subsets expressing markers of known cell function (Fig. 4A and Supplementary Fig. 7A): MDMs (*Apoe* and *Ctsd*), disease-associated MDMs (*Gpnmb* and *Spp1*), pro-inflammatory MDMs (*Fosb* and *Jun*), proliferating MDMs (*Top2a* and *Stmn1*), disease-associated monocytes (*Arg1* and *Hilpda*), homeostatic monocytes (*S100a4* and *S100a6*), pro-inflammatory monocytes (*Il1b* and *Fn1*) and Interferon-responsive monocytes/MDMs (*Cxcl9* and *Cxcl10*). Furthermore, we explored the monocyte and MDM cell-state transitions in our data using RNA velocity (Fig. 4A). Trajectory inference suggested a transition from proliferating to pro-inflammatory cell subsets that eventually converged to disease-associated and interferon-responsive monocytes/MDMs.

Examining the cell subset distribution in our three mGBM models, we found a higher relative proportion of MDMs in *Nf1* mGBM, of proliferative MDMs in *EGFRvIII* mGBM and of monocytes in the PDGFB mGBM subtype (Fig. 4B and C). The higher ratio of monocytes to MDMs in PDGFB mGBM compared with *Nf1* mGBM might occur, in part, owing to a more permeable vasculature in PDGFB mGBM and PN hGBM compared with *Nf1* mGBM and MES hGBM.^{19,49} Additionally, the increased proliferation of MDMs within the *Nf1* mGBM might also play a role. As a complementary analysis to Louvain clustering, we again used hdWGCNA to identify *de novo* 26 monocyte and MDM gene expression programmes (Supplementary Table 5), which varied in their activity between our mGBM GEMMs (Fig. 4D and Supplementary Fig. 7B). We found TNF signalling to be elevated in the *Nf1* mGBM subtype, whereas *EGFRvIII* mGBM showed increased expression of interferon signalling in monocytes and MDMs. Interestingly, we uncovered a hypoxia programme that was elevated in *EGFRvIII* mGBM and PDGFB mGBM. Hypoxia plays a pivotal role in tumour progression by destabilizing endothelial junctions and contributing to hyperpermeable tumour vasculature.⁵² In sum, we find increased hypoxia and monocyte-to-MDM ratio in PDGFB mGBM, which might be related to a more permeable vasculature previously reported in this GBM subtype.

To elucidate the mechanisms driving myeloid phenotypic differences between mGBM subtypes, we inferred ligand–receptor interactions between MDMs/monocytes and all other cell types.³² For *EGFRvIII* mGBM, we see enriched interactions between *Egfr*-expressing tumour cells and monocytes/MDMs expressing *Tgfb1*, *Copa* and *Gri* (Supplementary Fig. 8A). This is likely to be attributable to elevated expression of *Egfr*/*EGFR* observed in *EGFRvIII* mGBM and hGBM (Supplementary Fig. 8B). Interestingly, consistent with the increased fraction of disease-associated MDMs in *Nf1* mGBM (Fig. 4C), we also observed an enrichment of cell interactions involving *Spp1* (osteopontin) and multiple receptors (*Cd44*, *Ptger4* and integrins) between monocytes and other cell types (Fig. 4E and Supplementary Fig. 8A). The myeloid expression of SPP1 is correlated with immunosuppression, macrophage infiltration, tumour progression and poor prognosis in GBM.⁵³ Our hGBM validation cohort also showed elevated expression of SPP1, CD44 and PTGER4 in *NF1*-mutant tumours (Fig. 4F). We also performed IHC analysis on five tumours per GEMM with antibodies against SPP1 and CD44, which demonstrated higher expression of SPP1 and CD44 in *Nf1* mGBM, validating our results at the protein level (Fig. 4G and H). This analysis highlights the subtype-specific context of therapeutically relevant interactions involving MDMs/monocytes within the TME and suggests that targeting the

SPP1–CD44 axis⁵⁴ might represent a promising therapeutic avenue in *NF1*-mutant GBM.

Characterizing neutrophil subsets and cell-state transitions in mGBM

Neutrophils have been shown to play a pivotal role in tumour progression and therapeutic response,^{55–58} emphasizing the necessity for a deeper understanding of their role in the mGBM TME. We explored the heterogeneity of neutrophils in GBM by annotating eight neutrophil subsets based on consistent expression of established functional markers, which consisted of activated (*Retnlg* and *Lcn2*), *Adrb2*-expressing (*Adrb2* and *Dynll1*), hypoxic (*Fnlp2* and *Vegfa*), interferon-responsive (*Ifit1* and *Ifit3*), macrophage-like (*C1qc* and *C1qa*), monocyte-like (*S100a4* and *Ccr2*), ribosome-expressing (*Rps27l* and *Rpl12*) and inflammatory neutrophils (*Cxcl2* and *Cxcl3*; Fig. 5A and B). We observed a higher relative fraction of monocyte-like, interferon-responsive and inflammatory neutrophils in PDGFB, *EGFRvIII* and *Nf1* mGBM, respectively (Supplementary Fig. 9A), which was consistent with increased monocyte abundance, interferon and TNF α signalling we noted in the MG and MDMs compartments for the respective mGBM subtypes (Fig. 4C and D and Supplementary Fig. 6B–D).

To investigate cell-state dynamics between the annotated neutrophil subsets, we again used RNA velocity.⁴⁷ We observed a transition from activated and macrophage-like to inflammatory neutrophils, which then converged to hypoxic neutrophils expressing *Vegfa* (Fig. 5C). To investigate the presence of hypoxic neutrophil subsets at the protein level, we performed Haematoxylin and Eosin staining and IHC on PDGFB-driven mGBM tumour samples using antibodies against hypoxia inducible factor-1 α (HIF-1 α) and endothelial cell marker CD31 (Supplementary Fig. 9B). High-resolution Haematoxylin and Eosin images illustrate the pseudopalisading structures, which consist of a rim and a necrotic core (Supplementary Fig. 9C). Whole scan images of the tumour show that the rim of the pseudopalisading areas is positive for HIF-1 α , indicating a decrease in the CD31-positive vascular regions (Supplementary Fig. 9B). We next stained sections for the neutrophil marker ELANE, the pan macrophage marker IBA1, and the hypoxia markers glucose transporter-1 (GLUT1) and hypoxia inducible factor-1 α (HIF-1 α). HIF-1 α and GLUT1-positive areas (rims) surround ELANE-positive neutrophils (necrotic core), supporting the presence of neutrophils in hypoxic areas in our GEMM scRNA-seq data (Fig. 5D). The expression of GLUT1 in glioblastomas has also been reported to be correlated with HIF-1 α expression at the rim of pseudopalisading regions,⁵⁹ and the presence of neutrophils in necrotic areas has been demonstrated in both human and murine GBM models.^{23,60} Interestingly, these neutrophils in the hypoxic zones are also surrounded by the tumour-associated macrophages, as shown by the IBA-1 staining (Fig. 5D).

Elevated regulatory T-cell abundance and CTLA4 expression in *Nf1* mGBM

Lymphocytes are crucial players in curbing tumour progression and enhancing therapeutic response, where increased CD3⁺ T-cell infiltration in GBM biopsies was linked to prolonged patient survival.⁶¹ To investigate the heterogeneity of lymphocytes within the mGBM TME, we first separated B (*Cd79a*; Supplementary Fig. 10A), plasma (*Jchain*), T (*Cd3e*) and NK (natural killer; *Klrk1*) cell clusters by coherent expression of established markers. Subsequently, we classified T-cell clusters into Cd4 and Cd8 classes, and further delineated

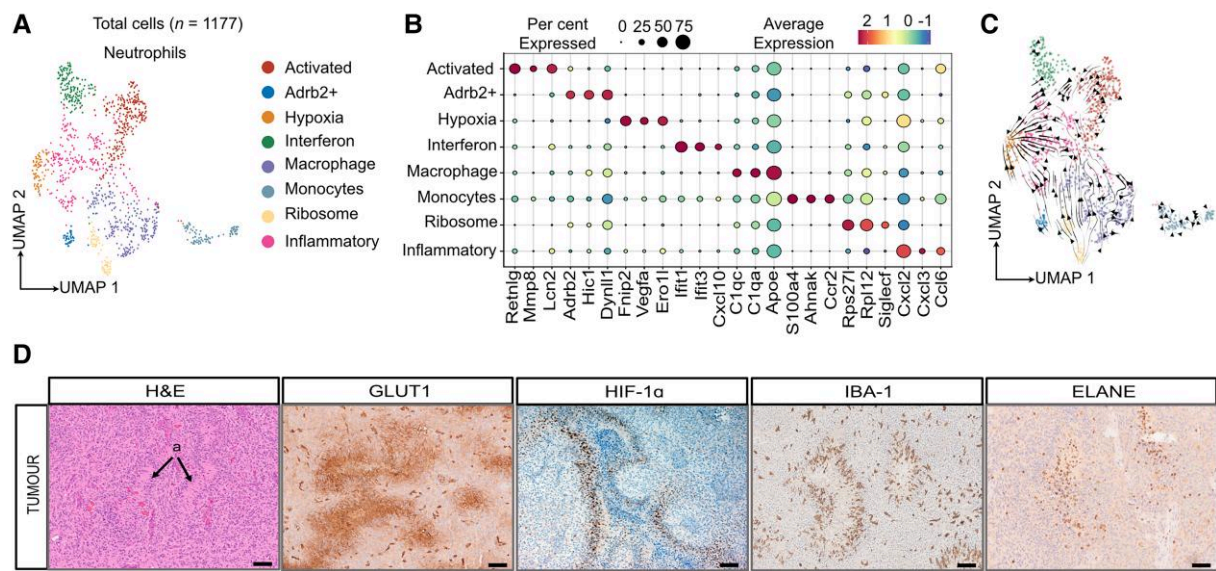


Figure 5 Characterization of neutrophil subsets and cell-state transitions in murine glioblastoma. (A) Uniform manifold approximation and projection (UMAP) plot of all sequenced murine glioblastoma (mGBM) neutrophils, coloured by subset annotations. (B) Dot plot showing expression levels and the percentage of cells expressing selected marker genes for each annotated cell subset. (C) UMAP plot of the RNA velocity cell-state transition in mGBM neutrophil cells, coloured by neutrophil subset annotations. (D) Left: Haematoxylin and eosin staining of a PDGFB-driven mGBM sample shows representative pseudopalisading areas (marked by black arrows) consisting of the hypoxic rim and necrotic core. Right: Immunohistochemical staining of serial sections for pan macrophage marker IBA-1, hypoxia markers glucose transporter-1 (GLUT1) and hypoxia-inducible factor-1a (HIF-1a), which all stained the rims of various pseudopalisading areas, and neutrophil marker elastase (NE) enriched in the necrotic core. Scale bars: 100 µm.

T-cell subsets within them based on lineage and functional markers (Fig. 6A and B), which included effector (*Gzmk* and *S100a4*), exhausted (*Tox* and *Pdcd1*), gamma delta (*Trdc* and *Tcrg-C1*), interferon signalling (*Ifit1* and *Ifit3*), memory (*Lnpep* and *Mycbp2*), naïve (*Tcf7* and *S1pr1*), regulatory (*Foxp3* and *Ctla4*), *Ccl4*-expressing (*Ccl4* and *Nfkb1*) and proliferating (*Mki67* and *Top2a*) T-cell subsets (Fig. 6A and B). When comparing the lymphocyte composition in our three GEMMs, we observed higher relative abundance of B cells in *Nf1* mGBM, NK cells in PDGFB mGBM and T cells in *Nf1* and PDGFB mGBM, respectively (Fig. 6C and D and Supplementary Fig. 10B). We validated these findings across a larger cohort using multicolour flow cytometry (Fig. 6E). These trends were also highly concordant with T-cell expression modules discovered in our scRNA-seq data using hdWGCNA (Supplementary Table 6 and Supplementary Fig. 10C and D).

Interestingly, when examining T-cell subsets, we observed an enrichment of regulatory T cells in *Nf1* mGBM in both our scRNA-seq and flow cytometry data (Fig. 6D and E, right panels). Cytotoxic T-lymphocyte antigen 4 (CTLA4), when expressed on the surface of regulatory T cells, competes with CD28 for binding to co-stimulatory molecules CD80 and CD86 expressed on antigen-presenting cells, thereby inhibiting activation of T cells.⁶² In agreement with higher regulatory T-cell content, *Nf1* mGBM displayed increased T-cell expression of *Ctla4* relative to other mGBM subtypes (Fig. 6F). Moreover, CTLA4 expression was also elevated in hGBM *NF1*-mutant tumours from our validation cohort (Fig. 6G). This observation is supported by the recent report demonstrating how blocking αCTLA-4, specifically in mesenchymal-like GBM, stimulates a CD4⁺ T cell-microglia circuit. This leads to activation of microglia and phagocytosis driven by IFN γ . The activated microglia then act as antigen-presenting cells, stimulating the CD4⁺ T-cell response, leading to improved survival of tumour-bearing mice.⁶³ Taken together, we find an enrichment of regulatory T cells and

CTLA4 expression in *Nf1* mGBM, suggesting that anti-CTLA4 immunotherapy might be well suited for patients with *NF1*-mutant hGBM.

Genotype-specific stromal and endothelial cell heterogeneity in mGBM

TME stromal cells, including cancer-associated fibroblasts (CAFs), play an important role in tumour invasion, metastasis and drug resistance. Moreover, targeting CAFs therapeutically can enhance cancer treatment efficacy.⁶⁴ In GBM, CAF abundance (<5% of tumour mass) is correlated with MES subtype, higher tumour grades and poor clinical outcomes.⁶⁵ To investigate the role of different genetic drivers on GBM stromal heterogeneity, we clustered all stromal cells and identified four distinct subsets expressing established markers: fibroblasts (*Col1a1*), pericytes (*Higd1b*), smooth muscle (*Acta2*) and proliferating cells (*Mki67*; Fig. 7A and B). Subsequently, we quantified stromal cell compositions for different mGBM subtypes and observed enrichment of fibroblasts in PDGFB mGBM, pericytes in *Nf1* mGBM and smooth muscle and stromal proliferating cells in EGFRvIII mGBM (Fig. 7C and D). Our stromal subset annotations and enrichments for mGBM subtypes were highly consistent with subset signatures from previously characterized CNS fibroblasts⁶⁶ (Supplementary Fig. 11A).

A recent study uncovered that high expression of TGF β contributes to the development of a dense extracellular matrix, consequently hindering T-cell migration to the tumour core. Furthermore, the blockade of Tgf β and PD-L1 significantly enhances T-cell infiltration and promotes tumour regression.⁶⁷ Notably, we observed that *Nf1* mGBM tumours have a higher expression of Tgf β 1 in stromal cells in comparison to other mGBM subtypes (Supplementary Fig. 11B), consistent with a more invasive phenotype of this subtype.⁶⁸ In agreement, TCGA bulk RNA-seq

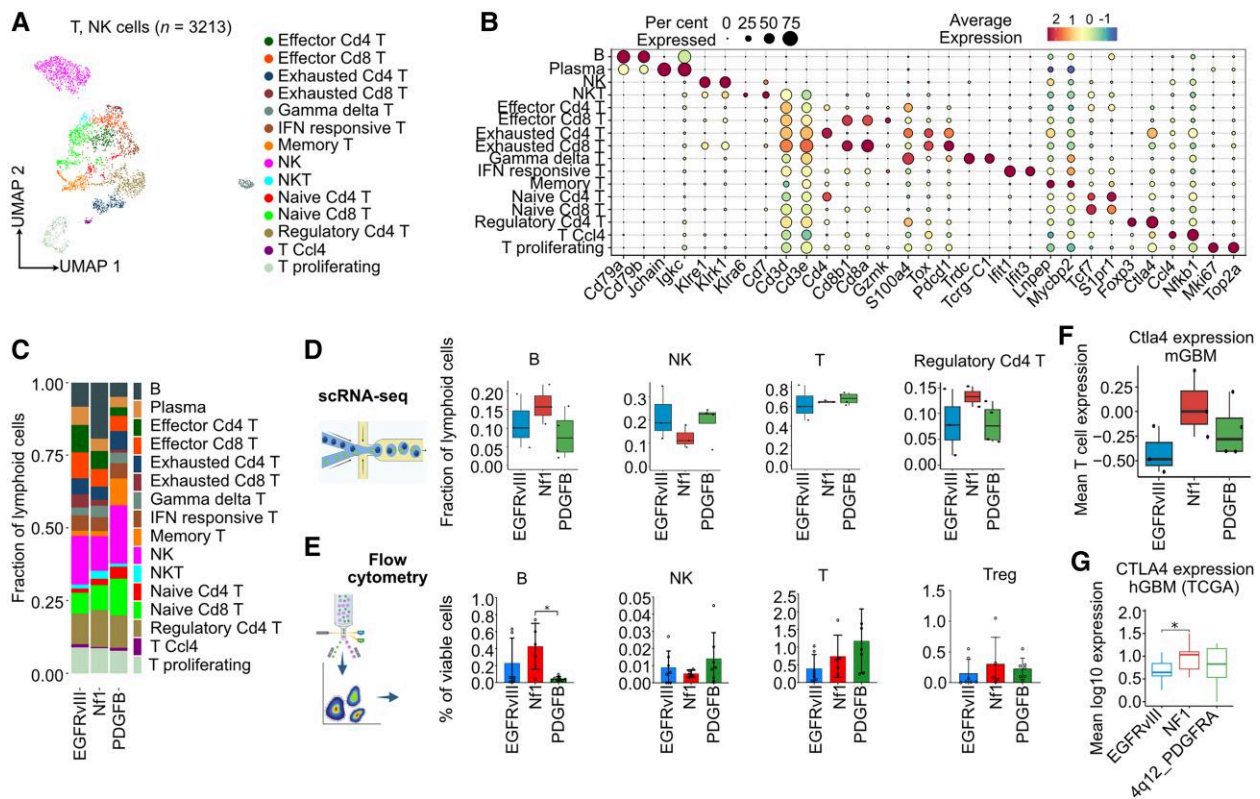


Figure 6 Elevated regulatory T-cell abundance and CTLA4 expression in *Nf1* murine glioblastoma. (A) Uniform manifold approximation and projection (UMAP) plot of all sequenced murine glioblastoma (mGBM) T and natural killer (NK) cells, coloured by cell subset annotations. (B) Dot plot showing expression levels and the percentage of cells expressing selected marker genes for each annotated lymphocyte subset. (C) Stacked bar plots depicting the proportion of lymphocyte cell subsets for each mGBM genetically engineered mouse model (GEMM). (D) Distribution of B-, NK-, T- and regulatory T-cell proportions relative to all lymphocytes. The t-test P-values were calculated, with blue = EGFRvIII, red = *Nf1* and green = PDGFB. Box plots display the median (central line) and interquartile range (box), with whiskers extending to the smallest and largest values within 1.5 times the interquartile range. Individual data points are shown as dots, providing a detailed view of the sample distribution. (E) Flow cytometry analysis of B-, NK-, T- and regulatory T-cell proportions relative to all cells in mGBM samples. The t-test P-values were calculated. EGFRvIII is blue, *Nf1* is red, and PDGFB is green. Box plots display the median (central line) and interquartile range (box), with whiskers extending to the smallest and largest values within 1.5 times the interquartile range. Individual data points are shown as dots, providing a detailed view of the sample distribution. (F) Average *Ctla4* gene expression (log) in T cells, split by mGBM genotype, with Mann–Whitney–Wilcoxon test P-values calculated. Blue = EGFRvIII, red = *Nf1* and green = PDGFB. Box plots display the median (central line) and interquartile range (box), with whiskers extending to the smallest and largest values within 1.5 times the interquartile range. Individual data points are shown as dots, providing a detailed view of the sample distribution. (G) Mean log₁₀ expression of *CTLA4* gene, split by genotype in human glioblastoma (hGBM) TCGA data, with Mann–Whitney–Wilcoxon test P-values calculated. Blue = EGFRvIII, red = *NF1* and green = 4q12_PDGFB. Significance annotation: **P* < 0.05, ***P* < 0.01, ****P* < 0.001 and *****P* < 0.0001. P-values > 0.05 are not shown. Box plots display the median (central line) and interquartile range (box), with whiskers extending to the smallest and largest values within 1.5 times the interquartile range. Points beyond this range are potential outliers and are shown as individual dots.

data showed that expression of TGFβ1 ligand was highest in *NF1*-mutant hGBM (Supplementary Fig. 11C). This observation suggests that blocking TGFβ1 might enhance anti-tumour immune responses in *NF1*-mutant GBM.

GBM is highly angiogenic, and endothelial cells (ECs) are a key cellular component of the blood–brain barrier. We have previously observed that *Nf1* mGBM exhibits reduced vessel size and positive area, in addition to decreased permeability in comparison to PDGFB mGBM, similar to the corresponding subtypes in humans.¹⁹ However, there remains limited knowledge about the heterogeneity of ECs and their association with different GBM genetic drivers. We identified eight EC subsets in mGBM, including *Lars2*⁺ (*Lars2*), large vein (*Ackr1*), *Cxcl12*⁺ (*Cxcl12*), proliferating (*Top2a*), *Angpt2*⁺ (*Angpt2*), interferon-responsive (*Cxcl9*), capillary/venous (*Slc16a1*) and choroid plexus (*Plvap*) ECs (Fig. 7E and F). Comparing EC composition between GEMMs of GBM, we observed that choroid plexus, interferon-responsive and large vein ECs were enriched in EGFRvIII mGBM, whereas *Cxcl12*⁺ and capillary/venous ECs were elevated in

Nf1 mGBM (Fig. 7G and H). Additionally, *Lars2*⁺, *Angpt2*⁺ and proliferating ECs were increased in PDGFB mGBM.

Although we observed variation between different stromal subsets, we noted that *Nf1* mGBM displayed the highest abundance of ECs relative to other mGBM subtypes (Fig. 7I), which was consistent with bulk deconvolution analysis in hGBM RNA-seq data from TCGA (Fig. 7J). This implies an elevated vascularization and supply of oxygen in *Nf1* mGBM, which might explain the reduced hypoxia observed in MDM and MG in this subtype (Fig. 4D and Supplementary Fig. 6B).

Discussion

By combining scRNA-seq of immunocompetent GEMMs with in-depth computational analysis, we comprehensively characterized the TME differences associated with EGFRvIII and PDGFB oncogenic drivers and tumour suppressor *Nf1* in mGBM. Although these

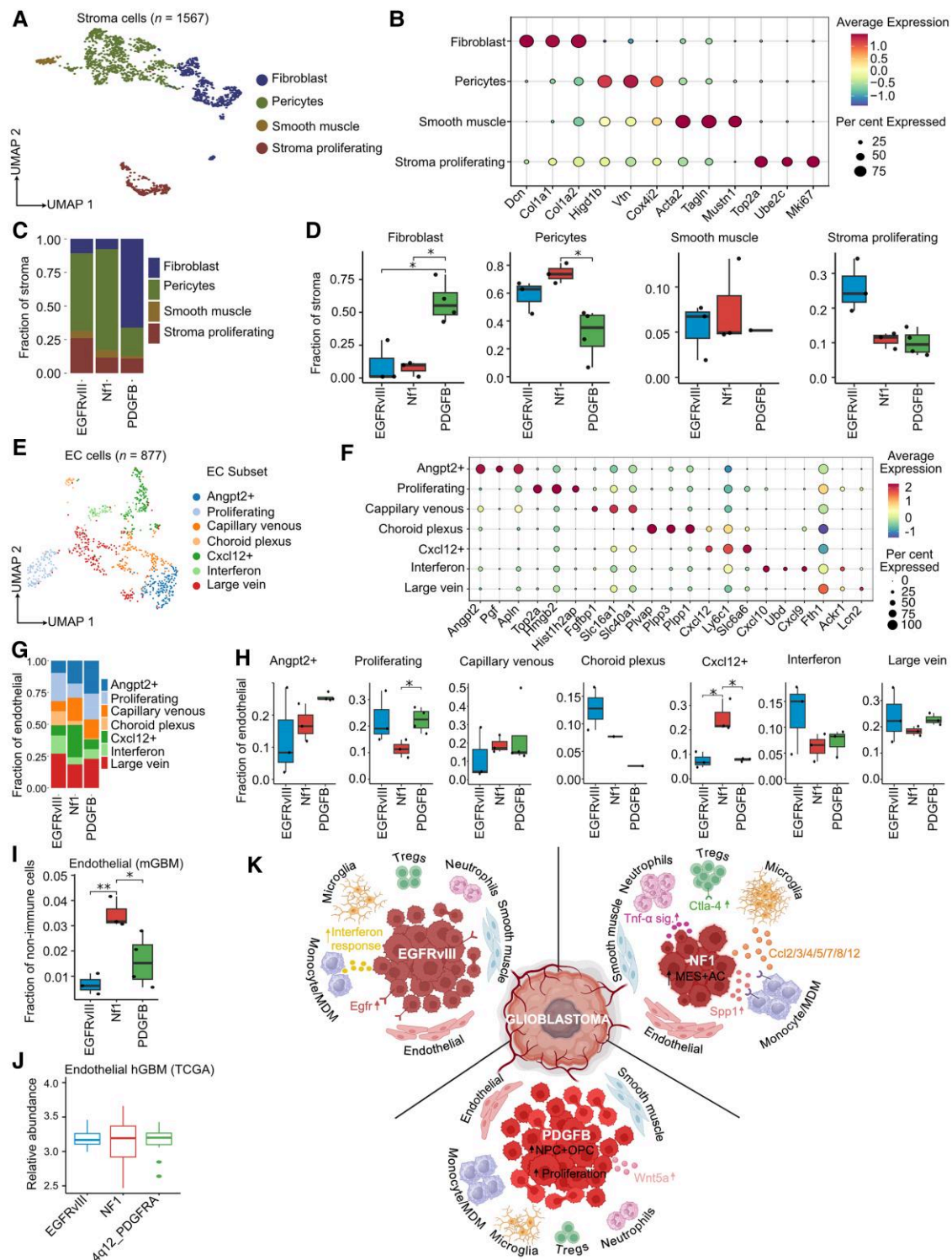


Figure 7 Genotype-specific stromal and endothelial cell heterogeneity in murine glioblastoma. (A) Uniform manifold approximation and projection (UMAP) plot of all sequenced murine glioblastoma (mGBM) stromal cells, coloured by subset annotations. (B) Dot plot showing expression levels and the percentage of cells expressing selected marker genes for each annotated cell subset. (C) Stacked bar plots depicting the proportion of stromal cell subsets within each mGBM GEMM. (D) Distribution of stromal cell subset proportions grouped by mGBM genotypes. The t-test P -values were calculated, with blue = EGFRvIII, red = NF1 and green = PDGFB. Box plots display the median (central line) and interquartile range (box), with whiskers extending to the smallest and largest values within 1.5 times the interquartile range. Individual data points are shown as dots, providing a detailed view of the sample distribution. (E) UMAP plot of all sequenced mGBM endothelial cells (ECs), coloured by subset annotations. (F) Dot plot showing expression levels and the percentage of cells expressing selected marker genes for each annotated cell subset. (G) Stacked bar plots depicting the proportion of EC subsets within each mGBM genetically engineered mouse model (GEMM). (H) Distribution of EC subset proportions grouped by mGBM genotypes. The t-test P -values were calculated, with blue = EGFRvIII, red = NF1 and green = PDGFB. Box plots display the median (central line) and interquartile range (box), with whiskers extending to the smallest and largest values within 1.5 times the interquartile range. Individual data points are shown as dots,

(Continued)

GEMMs have previously been shown closely to resemble the transcriptional profiles of hGBM CL, MES and PN subtypes,^{16–19} respectively, a direct link between genetic drivers and the TME has not been established previously. Although there are several other Cre-Lox recombination-based^{69–72} and viral-induced^{73,74} genetic GBM models available, we used the RCAS/tv-a system in this study, which ensured the same cell of origin of different GEMMs and enabled us to isolate the effect of driver mutations on tumour heterogeneity as a primary variable. Our computational approach identified cell subset compositions, gene modules, ligand–receptor interactions and cell-state trajectories that differed between the different models. For validation of the key findings, we used IHC and multicolour flow cytometry in addition to comparison with human bulk RNA-seq data¹² from tumours with similar genetic alterations for assessment of human relevance. This human–mouse comparison enabled data-driven discovery of human-relevant GBM therapeutic targets and provides the appropriate murine model for preclinical validation in different contexts.

Through this systematic dissection of the TME, where we focused on highlighting cross-species similarities while also enumerating species differences, we demonstrated that PDGFB mGBM tumours are more proliferative than EGFRvIII or Nf1 mGBM tumours. We believe this is attributable, in part, to increased WNT signalling interactions involving neoplastic cells and higher expression of the ligands WNT7B, WNT5A and receptor LRP5, where the latter two were validated by IHC. PDGFB mGBM is also marked by the highest presence of NPC- and OPC-like cancer cell states, in both mGBM and hGBM tumour data. We also observed a more hypoxic myeloid compartment and an elevated ratio of monocytes to MDMs in PDGFB mGBM, which is likely to be related to a more permeable vasculature previously reported in this GBM subtype.^{19,49} This underscores the complexity in cellular interactions between tumour, stromal and immune cells that shape the distinct TME (Fig. 7K).

In contrast, Nf1 mGBM tumours had a higher relative abundance of AC- and MES-like cancer cells, in addition to MDMs, MG and neutrophils in both murine and human GBM, in line with this mutation being enriched in the MES GBM subtype.^{15,16} The elevated myeloid content is attributable, in part, to increased expression of MCP family ligands in myeloid cells we observed in Nf1 mGBM. Moreover, the higher myeloid abundance was accompanied by an enrichment of immunosuppressive interactions involving osteopontin (Spp1) and its receptors in monocytes and MDMs, which was supported by IHC. Nf1 mGBM was also associated with elevated levels of regulatory T cells and expression of the immune checkpoint molecule Ctl4 (Fig. 7K). The enrichments of the SPP1–CD44 and CTLA4–CD80/86 pathways were highly consistent in our human validation cohort, implying that therapeutic targeting of these interactions might be a viable strategy in NF1-mutant hGBM.^{54,63}

EGFRvIII mGBM tumours displayed intermediate levels of enrichment for tumour cell proliferation and for NPC/OPC- and AC/

MES-like cancer cell states in comparison to PDGFB and Nf1 mGBM. The TME of EGFRvIII mGBM was marked by the lowest abundance of myeloid subsets and expression for MCP chemokines. Despite the lowest myeloid content, we observed the highest relative amount of proliferating MG and MDMs in EGFRvIII mGBM. Interestingly, we also observed the highest interferon signalling response in EGFRvIII mGBM across most cellular compartments, including in cancer cells, MDM, MG, neutrophils and endothelial cells (Fig. 7K). Strong correlation between activation of the EGFR pathway and the IFN- γ pathway was also shown in hGBM, which was also associated with a poorer prognosis and a more immunosuppressive TME.⁷⁵

Furthermore, our comprehensive data set and systematic annotation allowed us to characterize the mGBM TME in greater detail. We identified 54 non-neoplastic cell subsets in mGBM and inferred the cell-state transitions between these subsets using RNA velocity. This analysis implied a cell-state trajectory towards inflammatory MG and disease-associated MDMs in the myeloid compartments. Of interest to us, we also found a convergence of neutrophil subsets towards hypoxic neutrophils expressing Vegfa and confirmed the presence of this subset using IHC mainly in pseudopalisading necrotic areas. These results are in line with previous reports showing that neutrophils coincide with necrosis temporally and spatially and that neutrophil depletion dampened necrosis in GBM patient derived xenograft mouse models.⁶⁰ Our fully annotated data set represents the most complete single-cell resource of mGBM to date and is available to the GBM community for future exploration via the web-enabled CellxGene portal (<https://cellxgene.cziscience.com/collections/6d7d23d0-237d-4430-9200-92858abba2d8>).

Despite decades of research in myeloid biology in GBM, we still do not have effective therapies to target these cells. Results from myeloid targeting in the literature suggest a potentially high degree of tumour genotype-dependent heterogeneity of myeloid cells that should be considered carefully. For instance, CSF1R1 inhibitors effectively targeted TAMs and prolonged survival in a PDGFB mGBM model.⁷⁶ However, targeting CSF1R1 did not show any effectiveness in an Nf1 mGBM model.⁷⁷ Clinical trials on unselected human adult recurrent GBM patients also indicated that CSF1R inhibitors failed to demonstrate efficacy.⁷⁸ Different results regarding the role of myeloid TREM2 in GBM can probably also be explained by genotype-dependent effects. TREM2 deficiency in myeloid cells reduced tumour growth in the SB28 (NRas/shTp53/mPDGF) and NPA C54B (NRas/shTp53/shATRX) syngeneic mouse models,⁷⁹ but not in GL261 or CT2A syngeneic models.^{80,81} Although similar responses in SB28 and NPA C54B can be attributed to their Ras driver mutation, differences in response to myeloid TREM2 targeting among various mouse models suggest that targeting TREM2 will probably yield disappointing outcomes in genetically heterogeneous hGBM patients, similar to those of CSF1R1 inhibitors and others.⁷⁸ Similar discrepancies were also observed with the role of myeloid-derived IL-1b. Targeting of IL-1B was effective in GL261

Figure 7 Continued

providing a detailed view of the sample distribution. (I) Distribution of endothelial cell proportions amongst non-immune cells for each mGBM GEMM. The t-test P-values were calculated, with blue = EGFRvIII, red = Nf1 and green = PDGFB. Box plots display the median (central line) and interquartile range (box), with whiskers extending to the smallest and largest values within 1.5 times the interquartile range. Individual data points are shown as dots, providing a detailed view of the sample distribution. (J) Mean \log_{10} expression of endothelial markers, split by genotype in human glioblastoma (hGBM) TCGA data, with Mann–Whitney–Wilcoxon test P-values calculated. Blue = EGFRvIII, red = NF1 and green = 4q12_PDGFRA. Significance annotation: *P < 0.05, **P < 0.01, ***P < 0.001 and ****P < 0.0001. P-values > 0.05 are not shown. Box plots display the median (central line) and interquartile range (box), with whiskers extending to the smallest and largest values within 1.5 times the interquartile range. Points beyond this range are potential outliers and are shown as individual dots. (K) Illustration of the distinct tumour microenvironments linked to different genetic drivers in mouse and human GBM. Created in BioRender. Rawat, K. (2025) <https://BioRender.com/qu334xc>.

and CT-2A syngeneic transplantable models,⁸² but in *de novo* RCAS/tva-based tumour models, targeting IL-1b showed efficacy in PDGFB mGBM but not in Nf1 mGBM models.²⁴ These findings indicate that the genetic make-up of a tumour influences the efficacy of different treatment strategies and demonstrates the importance of gaining a deeper understanding of how myeloid heterogeneity and function vary depending on genotype. Our work provides the scientific community with tools for rational, data-driven identification of targets and offers models for preclinical validation in the relevant genetic context.

Conclusion

In summary, our research systematically dissects the genotype-to-immunophenotype relationship in the mGBM TME and suggests context-specific, personalized therapeutic targets. This work paves the way for developing immunotherapeutic strategies tailored to the distinct subgroups characterized by NF1, EGFR and PDGFB genotypes in glioblastoma.

Data availability

All scRNA-seq data are available for download, exploration and analysis using the web-enabled CellxGene portal at <https://cellxgene.cziscience.com/collections/6d7d23d0-237d-4430-9200-92858abba2d8>. We have also deposited all raw data in the Gene Expression Omnibus (GEO) database under accession number GSE274339.

Acknowledgements

We thank all members of the Tsankov and Hambardzumyan laboratory for their scientific feedback. We would like to acknowledge the ISMMS Genomics Core for help with single-cell profiling and sequencing of GBM tumour samples, the Neuropathology brain bank and research core and the Mount Sinai Flow Cytometry core. This work was supported in part through the computational and data resources and staff expertise provided by Scientific Computing and Data at the Icahn School of Medicine at Mount Sinai and supported by the Clinical and Translational Science Awards (CTSA) grant UL1TR004419 from the National Center for Advancing Translational Sciences. Graphical elements used to create experimental design schemes were generated using a licensed version of BioRender. The thumbnail image for the online table of contents was Created in BioRender. Tsankov, A. (2025) <https://BioRender.com/3hk9rwx>.

Funding

This work was supported by National Institutes of Health (R01NS100864, R01NS137631 and R01NS124159) funding (D.H.) and Icahn School of Medicine at Mount Sinai seed funding (D.H. and A.M.T.).

Competing interests

The authors report no competing interests.

Supplementary material

[Supplementary material](#) is available at [Brain](#) online.

References

- Price M, Ryan K, Shoaf ML, et al. Childhood, adolescent, and adult primary brain and central nervous system tumor statistics for practicing healthcare providers in neuro-oncology, CBTRUS 2015–2019. *Neurooncol Pract.* 2024;11:5–25.
- Ostrom QT, Cioffi G, Gittleman H, et al. CBTRUS statistical report: Primary brain and other central nervous system tumors diagnosed in the United States in 2012–2016. *Neuro Oncol.* 2019; 21(Suppl 5):v1–v100.
- Zhao J, Chen AX, Gartrell RD, et al. Immune and genomic correlates of response to anti-PD-1 immunotherapy in glioblastoma. *Nat Med.* 2019;25:462–469.
- Bagley SJ, Logun M, Fraietta JA, et al. Intrathecal bivalent CAR T cells targeting EGFR and IL13Rα2 in recurrent glioblastoma: Phase 1 trial interim results. *Nat Med.* 2024;30:1320–1329.
- Tang F, Wang Y, Zeng Y, Xiao A, Tong A, Xu J. Tumor-associated macrophage-related strategies for glioma immunotherapy. *NPJ Precis Oncol.* 2023;7:78.
- Choi BD, Gerstner ER, Frigault MJ, et al. Intraventricular CARv3-TEAM-E T cells in recurrent glioblastoma. *N Engl J Med.* 2024;390:1290–1298.
- Hambardzumyan D, Gutmann DH, Kettenmann H. The role of microglia and macrophages in glioma maintenance and progression. *Nat Neurosci.* 2016;19:20–27.
- Friedmann-Morvinski D, Hambardzumyan D. Monocyte-neutrophil entanglement in glioblastoma. *J Clin Invest.* 2023; 133:e163451.
- Cancer Genome Atlas Research Network. Comprehensive genomic characterization defines human glioblastoma genes and core pathways. *Nature.* 2008;455:1061–1068.
- Verhaak RG, Hoadley KA, Purdom E, et al. Integrated genomic analysis identifies clinically relevant subtypes of glioblastoma characterized by abnormalities in PDGFRA, IDH1, EGFR, and NF1. *Cancer Cell.* 2010;17:98–110.
- Wang Q, Hu B, Hu X, et al. Tumor evolution of glioma-intrinsic gene expression subtypes associates with immunological changes in the microenvironment. *Cancer Cell.* 2017;32:42–56.e6.
- Brennan CW, Verhaak RG, McKenna A, et al. The somatic genomic landscape of glioblastoma. *Cell.* 2013;155:462–477.
- Patel AP, Tirosh I, Trombetta JJ, et al. Single-cell RNA-seq highlights intratumoral heterogeneity in primary glioblastoma. *Science.* 2014;344:1396–1401.
- Sottoriva A, Spiteri I, Piccirillo SG, et al. Intratumor heterogeneity in human glioblastoma reflects cancer evolutionary dynamics. *Proc Natl Acad Sci U S A.* 2013;110:4009–4014.
- Brennan C, Momota H, Hambardzumyan D, et al. Glioblastoma subclasses can be defined by activity among signal transduction pathways and associated genomic alterations. *PLoS One.* 2009;4: e7752.
- Herting CJ, Chen Z, Pitter KL, et al. Genetic driver mutations define the expression signature and microenvironmental composition of high-grade gliomas. *Glia.* 2017;65: 1914–1926.
- Lei L, Sonabend AM, Guarnieri P, et al. Glioblastoma models reveal the connection between adult glial progenitors and the proneural phenotype. *PLoS One.* 2011;6:e20041.
- Ozawa T, Riester M, Cheng YK, et al. Most human non-GCIMP glioblastoma subtypes evolve from a common proneural-like precursor glioma. *Cancer Cell.* 2014;26:288–300.
- Chen Z, Herting CJ, Ross JL, et al. Genetic driver mutations introduced in identical cell-of-origin in murine glioblastoma reveal distinct immune landscapes but similar response to checkpoint blockade. *Glia.* 2020;68:2148–2166.

20. Neftel C, Laffy J, Filbin MG, et al. An integrative model of cellular states, plasticity, and genetics for glioblastoma. *Cell*. 2019;178:835-849.e21.
21. Tirosh I, Venteicher AS, Hebert C, et al. Single-cell RNA-seq supports a developmental hierarchy in human oligodendroglioma. *Nature*. 2016;539:309-313.
22. Hambardzumyan D, Amankulor NM, Helmy KY, Becher OJ, Holland EC. Modeling adult gliomas using RCAS/t-va technology. *Transl Oncol*. 2009;2:89-95.
23. Chen Z, Soni N, Pinerio G, et al. Monocyte depletion enhances neutrophil influx and proneural to mesenchymal transition in glioblastoma. *Nat Commun*. 2023;14:1839.
24. Chen Z, Giotti B, Kaluzova M, et al. A paracrine circuit of IL-1 β /IL-1R1 between myeloid and tumor cells drives genotype-dependent glioblastoma progression. *J Clin Invest*. 2023;133:e163802.
25. Hao Y, Hao S, Andersen-Nissen E, et al. Integrated analysis of multimodal single-cell data. *Cell*. 2021;184:3573-3587.e29.
26. Crowell HL, Soneson C, Germain P-L, et al. Muscat detects subpopulation-specific state transitions from multi-sample multi-condition single-cell transcriptomics data. *Nat Commun*. 2020;11:6077.
27. Morabito S, Reese F, Rahimzadeh N, Miyoshi E, Swarup V. hdWGCNA identifies co-expression networks in high-dimensional transcriptomics data. *Cell Rep Methods*. 2023;3:100498.
28. Wu T, Hu E, Xu S, et al. clusterProfiler 4.0: A universal enrichment tool for interpreting omics data. *Innovation (Camb)*. 2021;2:100141.
29. Castiglioni A, Yang Y, Williams K, et al. Combined PD-L1/TGF β blockade allows expansion and differentiation of stem cell-like CD8 T cells in immune excluded tumors. *Nat Commun*. 2023;14:4703.
30. Efremova M, Vento-Tormo M, Teichmann SA, Vento-Tormo R. CellPhoneDB: Inferring cell-cell communication from combined expression of multi-subunit ligand-receptor complexes. *Nat Protoc*. 2020;15:1484-1506.
31. Gao J, Aksoy BA, Dogrusoz U, et al. Integrative analysis of complex cancer genomics and clinical profiles using the cBioPortal. *Sci Signal*. 2013;6:pl1.
32. Vento-Tormo R, Efremova M, Botting RA, et al. Single-cell reconstruction of the early maternal-fetal interface in humans. *Nature*. 2018;563:347-353.
33. Yu C-Y, Liang G-B, Du P, Liu Y-H. Lgr4 promotes glioma cell proliferation through activation of Wnt signaling. *Asian Pac J Cancer Prev*. 2013;14:4907-4911.
34. Kamran N, Chandran M, Lowenstein PR, Castro MG. Immature myeloid cells in the tumor microenvironment: Implications for immunotherapy. *Clin Immunol*. 2018;189:34-42.
35. Pang L, Khan F, Heimberger AB, Chen P. Mechanism and therapeutic potential of tumor-immune symbiosis in glioblastoma. *Trends Cancer*. 2022;8:839-854.
36. Read RD, Tapp ZM, Rajappa P, Hambardzumyan D. Glioblastoma microenvironment—From biology to therapy. *Genes Dev*. 2024;38:360-379.
37. Pombo Antunes AR, Scheyltjens I, Lodi F, et al. Single-cell profiling of myeloid cells in glioblastoma across species and disease stage reveals macrophage competition and specialization. *Nat Neurosci*. 2021;24:595-610.
38. Urbantat RM, Vajkoczy P, Brandenburg S. Advances in chemokine signaling pathways as therapeutic targets in glioblastoma. *Cancers (Basel)*. 2021;13:2983.
39. Hoeffel G, Chen J, Lavin Y, et al. C-Myb⁺ erythro-myeloid progenitor-derived fetal monocytes give rise to adult tissue-resident macrophages. *Immunity*. 2015;42:665-678.
40. Ajami B, Bennett JL, Krieger C, Tetzlaff W, Rossi FM. Local self-renewal can sustain CNS microglia maintenance and function throughout adult life. *Nat Neurosci*. 2007;10:1538-1543.
41. Gomez Perdiguero E, Klapproth K, Schulz C, et al. Tissue-resident macrophages originate from yolk-sac-derived erythro-myeloid progenitors. *Nature*. 2015;518:547-551.
42. Ginhoux F, Greter M, Leboeuf M, et al. Fate mapping analysis reveals that adult microglia derive from primitive macrophages. *Science*. 2010;330:841-845.
43. Kierdorf K, Erny D, Goldmann T, et al. Microglia emerge from erythromyeloid precursors via Pu.1- and Irf8-dependent pathways. *Nat Neurosci*. 2013;16:273-280.
44. Masuda T, Sankowski R, Staszewski O, Prinz M. Microglia heterogeneity in the single-cell era. *Cell Rep*. 2020;30:1271-1281.
45. Lin C, Wang N, Xu C. Glioma-associated microglia/macrophages (GAMs) in glioblastoma: Immune function in the tumor microenvironment and implications for immunotherapy. *Front Immunol*. 2023;14:1123853.
46. Sattiraju A, Kang S, Giotti B, et al. Hypoxic niches attract and sequester tumor-associated macrophages and cytotoxic T cells and reprogram them for immunosuppression. *Immunity*. 2023;56:1825-1843.e6.
47. La Manno G, Soldatov R, Zeisel A, et al. RNA velocity of single cells. *Nature*. 2018;560:494-498.
48. Chen Z, Feng X, Herting CJ, et al. Cellular and molecular identity of tumor-associated macrophages in glioblastoma. *Cancer Res*. 2017;77:2266-2278.
49. Chen Z, Ross JL, Hambardzumyan D. Intravital 2-photon imaging reveals distinct morphology and infiltrative properties of glioblastoma-associated macrophages. *Proc Natl Acad Sci U S A*. 2019;116:14254-14259.
50. Caverzán MD, Beaugé L, Oliveda PM, Cesca González B, Bühler EM, Ibarra LE. Exploring monocytes-macrophages in immune microenvironment of glioblastoma for the design of novel therapeutic strategies. *Brain Sci*. 2023;13:542.
51. Buonfiglioli A, Hambardzumyan D. Macrophages and microglia: The Cerberus of glioblastoma. *Acta Neuropathol Commun*. 2021;9:54.
52. Wang W, Li T, Cheng Y, et al. Identification of hypoxic macrophages in glioblastoma with therapeutic potential for vascular normalization. *Cancer Cell*. 2024;42:815-832.e12.
53. He C, Sheng L, Pan D, et al. Single-cell transcriptomic analysis revealed a critical role of SPP1/CD44-mediated crosstalk between macrophages and cancer cells in glioma. *Front Cell Dev Biol*. 2021;9:779319.
54. Wei J, Marisetty A, Schrand B, et al. Osteopontin mediates glioblastoma-associated macrophage infiltration and is a potential therapeutic target. *J Clin Invest*. 2019;129:137-149.
55. Quail DF, Joyce JA. The microenvironmental landscape of brain tumors. *Cancer Cell*. 2017;31:326-341.
56. Bertaute A, Truntzer C, Madkouri R, et al. Blood baseline neutrophil count predicts bevacizumab efficacy in glioblastoma. *Oncotarget*. 2016;7:70948-70958.
57. Fossati G, Ricevuti G, Edwards SW, Walker C, Dalton A, Rossi ML. Neutrophil infiltration into human gliomas. *Acta Neuropathol*. 1999;98:349-354.
58. Liang J, Piao Y, Holmes L, et al. Neutrophils promote the malignant glioma phenotype through S100A4. *Clin Cancer Res*. 2014;20:187-198.
59. Komaki S, Sugita Y, Furuta T, et al. Expression of GLUT1 in pseudopalisaded and perivascular tumor cells is an independent prognostic factor for patients with glioblastomas. *J Neuropathol Exp Neurol*. 2019;78:389-397.

60. Yee PP, Wei Y, Kim S-Y, et al. Neutrophil-induced ferroptosis promotes tumor necrosis in glioblastoma progression. *Nat Commun.* 2020;11:5424.
61. Kmiecik J, Poli A, Brons NH, et al. Elevated CD3⁺ and CD8⁺ tumor-infiltrating immune cells correlate with prolonged survival in glioblastoma patients despite integrated immunosuppressive mechanisms in the tumor microenvironment and at the systemic level. *J Neuroimmunol.* 2013;264:71-83.
62. Ribas A, Wolchok JD. Cancer immunotherapy using checkpoint blockade. *Science.* 2018;359:1350-1355.
63. Chen D, Varanasi SK, Hara T, et al. CTLA-4 blockade induces a microglia-Th1 cell partnership that stimulates microglia phagocytosis and anti-tumor function in glioblastoma. *Immunity.* 2023;56:2086-2104.e8.
64. Zhao Y, Shen M, Wu L, et al. Stromal cells in the tumor microenvironment: Accomplices of tumor progression? *Cell Death Dis.* 2023;14:587.
65. Galbo PM Jr, Madsen AT, Liu Y, et al. Functional contribution and clinical implication of cancer-associated fibroblasts in glioblastoma. *Clin Cancer Res.* 2024;30:865-876.
66. Dorrier CE, Jones HE, Pintarić L, Siegenthaler JA, Daneman R. Emerging roles for CNS fibroblasts in health, injury and disease. *Nat Rev Neurosci.* 2022;23:23-34.
67. Yang W, Liu S, Mao M, et al. T-cell infiltration and its regulatory mechanisms in cancers: Insights at single-cell resolution. *J Exp Clin Cancer Res.* 2024;43:1-18.
68. Kim Y, Varn FS, Park S-H, et al. Perspective of mesenchymal transformation in glioblastoma. *Acta Neuropathol Commun.* 2021;9:50.
69. Liu C, Sage JC, Miller MR, et al. Mosaic analysis with double markers reveals tumor cell of origin in glioma. *Cell.* 2011;146:209-221.
70. Zhu Y, Guignard F, Zhao D, et al. Early inactivation of p53 tumor suppressor gene cooperating with NF1 loss induces malignant astrocytoma. *Cancer Cell.* 2005;8:119-130.
71. Zhu H, Acquaviva J, Ramachandran P, et al. Oncogenic EGFR signaling cooperates with loss of tumor suppressor gene functions in gliomagenesis. *Proc Natl Acad Sci U S A.* 2009;106:2712-2716.
72. Chow LM, Endersby R, Zhu X, et al. Cooperativity within and among Pten, p53, and rb pathways induces high-grade astrocytoma in adult brain. *Cancer Cell.* 2011;19:305-316.
73. Friedmann-Morvinski D, Bushong EA, Ke E, et al. Dedifferentiation of neurons and astrocytes by oncogenes can induce gliomas in mice. *Science.* 2012;338:1080-1084.
74. Assanah M, Lochhead R, Ogden A, Bruce J, Goldman J, Canoll P. Glial progenitors in adult white matter are driven to form malignant gliomas by platelet-derived growth factor-expressing retroviruses. *J Neurosci.* 2006;26:6781-6790.
75. Zhou X, Liang T, Ge Y, Wang Y, Ma W. The crosstalk between the EGFR and IFN- γ pathways and synergistic roles in survival prediction and immune escape in gliomas. *Brain Sci.* 2023;13:1349.
76. Pyonteck SM, Akkari L, Schuhmacher AJ, et al. CSF-1R inhibition alters macrophage polarization and blocks glioma progression. *Nat Med.* 2013;19:1264-1272.
77. Chipman ME, Wang Z, Sun D, Pedraza AM, Bale TA, Parada LF. Tumor progression is independent of tumor-associated macrophages in cell lineage-based mouse models of glioblastoma. *Proc Natl Acad Sci U S A.* 2023;120:e2222084120.
78. Butowski N, Colman H, De Groot JF, et al. Orally administered colony stimulating factor 1 receptor inhibitor PLX3397 in recurrent glioblastoma: An Ivy Foundation Early Phase Clinical Trials Consortium phase II study. *Neuro Oncol.* 2015;18:557-564.
79. Sun R, Han R, McCornack C, et al. TREM2 inhibition triggers anti-tumor cell activity of myeloid cells in glioblastoma. *Sci Adv.* 2023;9:eade3559.
80. Peshoff MM, Gupta P, Oberai S, et al. Triggering receptor expressed on myeloid cells 2 (TREM2) regulates phagocytosis in glioblastoma. *Neuro Oncol.* 2024;26:826-839.
81. Zheng J, Wang L, Zhao S, et al. TREM2 mediates MHCII-associated CD4⁺ T-cell response against gliomas. *Neuro Oncol.* 2024;26:811-825.
82. Bayik D, Zhou Y, Park C, et al. Myeloid-derived suppressor cell subsets drive glioblastoma growth in a sex-specific manner. *Cancer Discov.* 2020;10:1210-1225.